INTERNATIONAL JOURNAL FOR NUMERICAL METHODS IN FLUIDS
Int. J. Numer. Meth. Fluids 2003; **42**:493–526 (DOI: 10.1002/fld.525)

A numerical study of the propulsive efficiency of a flapping hydrofoil

G. Pedro, A. Suleman*,† and N. Djilali

University of Victoria, Department of Mechanical Engineering, Victoria, BC, Canada V8W 3P6

SUMMARY

A computational fluid dynamics study of the swimming efficiency of a two-dimensional flapping hydrofoil at a Reynolds number of 1100 is presented. The model accounts fully for viscous effects that are particularly important when flow separation occurs. The model uses an arbitrary Lagrangian–Eulerian (ALE) method to track the moving boundaries of oscillatory and flapping bodies. A parametric analysis is presented of the variables that affect the motion of the hydrofoil as it moves through the flow along with flow visualizations in an attempt to quantify and qualify the effect that these variables have on the performance of the hydrofoil. Copyright © 2003 John Wiley & Sons, Ltd.

KEY WORDS: flapping hydrofoil; swimming propulsion; hydrofoil efficiency

1. INTRODUCTION

In aerodynamics and hydrodynamics, bird flight and fish swimming have inspired and guided the development of aircraft and underwater vehicles. It is interesting, however, to note how primitive these man-made machines seem compared to their natural counterparts in terms of intelligence, efficiency, agility, adaptiveness and functional complexity. These and other similar observations and issues have been addressed by the scientific community, have triggered the formulation of the science of biomimetics and have inspired new approaches to old problems. Problems in the self-propulsion of deformable bodies through fluids invite the co-operation of tools from structural mechanics, theoretical and experimental hydrodynamics, computational fluid dynamics and control theory, to name a few.

1.1. Background and motivation

The highly efficient swimming mechanisms of some fish can potentially provide inspiration for design of propulsive systems that will outperform the thrusters and propellers currently in

* Correspondence to: A. Suleman, Department of Mechanical Engineering, University of Victoria, P.O. Box 3055, Victoria, BC, Canada V8W 3P6.
† E-mail: suleman@uvic.ca

Received 14 January 2002
Revised 27 January 2003

use. The advantages of noiseless propulsion associated with a less conspicuous wake could be particularly useful for military applications. Thus, there is a need to further our knowledge of the hydrodynamics and fluid–structure interactions in fish swimming and to provide benchmarks for new theoretical developments and designs. Propulsion by means of oscillating hydrofoils has been the focus of considerable interest in recent years. Applications that could substantially benefit from this technology include autonomous underwater vehicles.

The flapping hydrofoil is the primary component in fish propulsion kinematics. The objective of this paper is to understand the hydrodynamics and fluid–structure interactions in pitching and heaving hydrofoils. In particular, the present work attempts to further our understanding of the mechanisms which affect thrust and efficiency by modelling the wake structure and its evolution. This research effort involves the development of computational methods and tools to simulate the fluid–structure interaction dynamics of a flapping hydrofoil, and the results are compared with benchmark experimental case studies reported in the literature. Furthermore, the present work represents a small but important step in a broad research program in the area of design of adaptive undersea vehicles that generate thrust using vorticity control mechanisms (i.e. flapping foil combined with body deformation).

1.2. Propulsion studies

Many researchers have addressed the problem of foil motion in the context of aerodynamic and hydrodynamic propulsion. In particular, the flapping foil propulsion, similar to the *thunniform* mode of propulsion, has received considerable attention in recent years. In *thunniform* propulsion, the caudal fin acts a the main propulsive element, providing up to 90% of the thrust. Researchers have attempted to formulate mathematical models to further understand the observed kinematics of fish. The flapping hydrofoil produces thrust as it oscillates developing a reverse Kármán vortex street (which has vortices rotating in opposite directions to the classical Kármán vortex street) that corresponds to a jet-like average velocity profile. However, such jets are convectively unstable and there is only a narrow bandwidth of frequencies for which the Kármán vortices and the jet-like profile co-exist and the flow is stable as demonstrated by Triantafyllou *et al.* [1]. Early hydrodynamic models were based on a quasi-static approach that uses steady-state flow theory to calculate the fluid forces for sequential frames of the motion. These models were restricted to simple body shapes and forms. Later models have dealt with more realistic assumptions. Lighthill [2] applied the slender body theory of hydrodynamics to transverse oscillatory motions of slender fish. This study revealed the high propulsive efficiency of fish, a finding that alone renders the utilization of similar propulsive techniques in man-made vehicles a very attractive quest. Other studies included analyses of a slender wing with passive chordwise flexibility [3], two-dimensional potential flow modelling over a thin waving plate of finite chord by Wu [4] and Siekmann [5], and a planar modelling of flow over a waving plate of finite thickness by Uldrick and Siekmann [6]. Wu not only studied the hydromechanics of swimming propulsion [7], he also researched optimum shape problems [8] and the hydromechanics of slender fish with side fins. Three-dimensional models have more recently been developed by Cheng *et al.* [9] and Bandyopadhyay *et al.* [10] who have utilized waving plate theory as well as comparisons of performance coefficients between fish and underwater vehicles.

Other researchers such as Isshiki and Murakami [11], Koochesfahani [12], Triantafyllou *et al.* [13] and Gopalkrishnan *et al.* [14] have addressed the problem of the thrust-producing capability of moving hydrofoils. Ramamurti *et al.* [15] studied flapping airfoils using an

incompressible flow solver. Tuncer and Platzer [16] also conducted a computational study of flapping airfoil dynamics.

In terms of experimental work, Anderson's PhD thesis [17] on vorticity control provides excellent data with which to compare results. The experimental work concentrated on the flow around pitching and heaving airfoils at a Reynolds number of 1100. Koochesfahani [18] also studied experimentally a pitching airfoil at a Reynolds number of 12 000. Robotuna [18], a robotic undersea vehicle, designed and constructed at the Massachusetts Institute of Technology (MIT) has demonstrated that *thunniform* propulsion is indeed very efficient. Robotuna achieved efficiencies on the order of 91%, not including losses in the actuators.

In this body of work, a computational fluid dynamics research code (CFDLIB, [19]) based on structured grids is used to study the unsteady flow past oscillating hydrofoils at low Reynolds numbers. The viscous flow past a NACA0012 hydrofoil at various pitching and heaving frequencies and other design parameters is simulated. The variation of the force coefficient with reduced frequency is compared to the experimental work published by Anderson. In all the numerical studies cited, it has been observed that the published data has failed to appropriately quantify the efficiency of the thrust producing hydrofoil. The present paper attempts to address this issue and presents a quantitative analysis on the efficiency of the flapping hydrofoil used in the *thunniform* mode of propulsion as a function of the Strouhal number which depends on the vortex shedding frequency and wake width.

1.3. Flow over static and oscillating cylinders

The unsteady viscous flow behind a circular cylinder has been the object of numerous experimental and numerical studies, especially from the fluid mechanics point of view, because of the fundamental mechanisms that this flow exhibits. A case that is often used to benchmark codes and that has been studied extensively is the oscillating cylinder.

Blackburn and Henderson [20] studied the flow past an oscillating cylinder utilizing a spectral method. They limited the oscillation amplitude to one case and studied the flow when the cylinder is oscillated at a frequency close to its shedding frequency. Mendes and Branco [21] applied their finite element code to a cylinder in cross-flow oscillation with a lower amplitude of motion as well as at a lower Reynolds number of 200. Koopman [22] conducted an experimental study of the wake geometry behind oscillating cylinders at low Reynolds numbers (100, 200 and 300). Tanida *et al.* [23] also conducted experimental research on the stability of circular cylinders in uniform flow or in the wake of another cylinder. Mittal and Tezduyar [24–26] developed a finite element code and studied various incompressible flow cases including oscillating cylinders and airfoils.

In this paper, the oscillating cylinder is used as a benchmark to validate the CFD code used. This benchmark tests the capacity of the CFD code to not only properly resolve unsteady flows as well as flows where there is boundary movement.

2. FLUID FLOW MODELLING

Unsteady viscous flow is governed by the continuity and Navier–Stokes equations:

$$\nabla \cdot (\rho \mathbf{u}) = 0 \tag{1}$$

$$\frac{\partial \rho \mathbf{u}}{\partial t} + \nabla \cdot (\rho \mathbf{u}\mathbf{u}) = -\nabla p + \nabla \cdot \Pi + \rho \mathbf{F} \tag{2}$$

The above equations express conservation of mass and momentum, respectively, and account for the spatial and temporal distributions of the velocity vector, $\mathbf{u}$, and the pressure field p. For an incompressible flow field, the density ρ is constant spatially and in time. Π is the deviatoric stress tensor in which are prescribed viscous stresses, turbulent stresses or elastic–plastic material deformation. $\mathbf{F}$ defines the body forces present.

A finite-volume discretization technique is used to reduce the set of differential equations given by Equations (1) and (2) into a system of algebraic equations corresponding to the nodes of the computational mesh.

To account for mesh movement, an arbitrary Lagrangian–Eulerian (ALE) formulation is used. In a Lagrangian formulation, the mesh moves such that the control volumes coincide with material volumes and there is no advection relative to it. In a purely Eulerian method, the mesh does not move and there is advection relative to it. The ALE method (see Reference [27]) combines these two, to allow for mesh movement, and not necessarily with the fluid flow. To do this, the hydrodynamic time-step is split into a Lagrangian phase and a rezone–remap phase. In the Lagrangian phase, the fluid dynamics is taken into account and the mesh moves with the fluid to a new position. In rezoning, a new mesh is defined and remapping is performed to transfer the state variables to this new mesh. The details of the ALE methodology are given in References [19, 27], and only an overview of the salient aspects of the numerical method are given here.

For the purpose of discretization, it is convenient to recast Equations (1) and (2) in their control volume formulation, namely:

$$\int_{S_a(t)} \rho(\mathbf{u} - \mathbf{u}_a)\mathbf{n}\, \mathrm{d}S = 0 \tag{3}$$

$$\frac{\mathrm{d}}{\mathrm{d}t}\int_{V_a(t)} \rho \mathbf{u}\, \mathrm{d}V + \int_{S_a(t)} \rho \mathbf{u}(\mathbf{u} - \mathbf{u}_a)\mathbf{n}\, \mathrm{d}S = -\int_{S_a(t)} p\mathbf{n}\, \mathrm{d}S + \int_{S_a(t)} \mathbf{n}\Pi\, \mathrm{d}S + \int_{V_a(t)} \rho \mathbf{F}\, \mathrm{d}V \tag{4}$$

This formulation accounts for an arbitrary moving control volume. $S_a(t)$ is the surface of the control volume $V_a(t)$. The outward unit normal to the surfaces is $\mathbf{n}$. The movement of the control volume is defined by $\mathbf{u}_a = \mathrm{d}\mathbf{x}_a/\mathrm{d}t$. In the use of these equations, conservation of volume is maintained:

$$\frac{\mathrm{d}V_a(t)}{\mathrm{d}t} = \int_{S_a(t)} \mathbf{u}_a \mathbf{n}\, \mathrm{d}S \tag{5}$$

Following the definition of Eulerian and Lagrangian formulations, one can expect that for a purely Lagrangian formulation $\mathbf{u}_a = \mathbf{u}$ and for a purely Eulerian formulation $\mathbf{u}_a = 0$.

Equations (3) and (4) are cast in a conservative form, and are a combination of the fluid dynamics (the Lagrangian phase) and the mesh movement (remapping). In the Lagrangian phase, one sets the volume velocity to be equal to the fluid velocity, i.e. $\mathbf{u}_a = \mathbf{u}$. Equation (4) becomes:

$$\frac{\mathrm{d}}{\mathrm{d}t}\int_{V_L} \rho \mathbf{u}\, \mathrm{d}V = -\int_{S_L} p\mathbf{n}\, \mathrm{d}S + \int_{S_L} \mathbf{n}\Pi\, \mathrm{d}S + \int_{V_L} \rho \mathbf{F}\, \mathrm{d}V \tag{6}$$

where V_L is the Lagrangian control volume and S_L its surface. The time derivatives refer to this volume. The distorted mesh obtained in the Lagrangian phase can be altered by remapping:

$$\frac{d}{dt}\int_{S_k} \rho \mathbf{u}_R \mathbf{n}\, dS = 0 \tag{7}$$

$$\frac{d}{dt}\int_{V_k} \rho \mathbf{u}\, dV - \int_{S_k} \rho \mathbf{u}\mathbf{u}_R \mathbf{n}\, dS = 0 \tag{8}$$

where $\mathbf{u}_R = \mathbf{u}_a - \mathbf{u}$ and is the mesh velocity relative to the Lagrangian frame. V_k is the control volume defined by the mesh velocity $\mathbf{u}_a$ with S_k being its surface. This control volume changes the mesh from its initial value V_L to its final one V_k^*. This method is known as integral remapping.

The flow solver used is CFDLIB, which uses a cell-centred, finite volume method with explicit time-stepping. The flow field is discretized using a central differencing method.

3. PERFORMANCE PARAMETERS

In the study of both the oscillating cylinder and flapping hydrofoil, several parameters are used to quantify the flow characteristics. In this section, these parameters are presented.

With both the cylinder and hydrofoil, drag and lift coefficients provide important data essential to this study:

$$C_D = \frac{D}{\frac{1}{2}\rho U^2 lb} \tag{9}$$

$$C_L = \frac{L}{\frac{1}{2}\rho U^2 lb} \tag{10}$$

where b is the span of the hydrofoil or cylinder which is set to 1 and l is a characteristic length. In the case of the cylinder, its diameter is used ($l = d$) while in the case of the hydrofoil the chord length is used ($l = c$). In both cases, the total lift and drag can be divided into its pressure (force due to pressure field) and viscous (force due to shear stress) components. This is done throughout the paper.

Since the hydrofoil's main task is to produce thrust, it is often more convenient to think in terms of thrust instead of drag. Thrust is equal but opposite in direction to the drag force, therefore one has

$$C_T = -C_D = \frac{T}{\frac{1}{2}\rho U^2 cb} \tag{11}$$

The average thrust is defined as

$$\langle T \rangle = \frac{1}{\tau}\int_0^\tau T\, dt \tag{12}$$

where τ is the signal period. As in the case of the waving plate, power can be defined as the amount of energy imparted to the airfoil for it to overcome the fluid forces:

$$P(t) = -L(t)\frac{\mathrm{d}h}{\mathrm{d}t} - M(t)\frac{\mathrm{d}\theta}{\mathrm{d}t} \tag{13}$$

where $M(t)$ is the moment created by the lift and drag forces at the pitching axis and is non-dimensionalized by

$$C_M = \frac{M}{\frac{1}{2}\rho U^2 c^2 b} \tag{14}$$

The sign on both terms (in Equation (13)) is negative as the lift force and moment are reaction forces created by the fluid as the airfoil moves through it. Power can also be averaged over time:

$$\langle P \rangle = \frac{1}{\tau}\int_0^\tau P\,\mathrm{d}t \tag{15}$$

and also non-dimensionalized:

$$C_P = \frac{P}{\frac{1}{2}\rho U^3 c b} \tag{16}$$

Efficiency is a measure of the energy lost in the wake versus energy used in creating the necessary thrust:

$$\eta = \frac{\langle T \rangle U}{\langle P \rangle} \tag{17}$$

The frequency and heave amplitude can be non-dimensionalized by using the following parameters. The first is the wave number k:

$$k = \frac{\omega c}{2U} = \frac{\pi f c}{U} \tag{18}$$

with a more indicative parameter being the Strouhal number which is based not only on the shedding frequency but also on the wake width. Since the wake width is difficult to determine, one can approximate it with the amplitude of motion of the hydrofoil:

$$St_h = \frac{2h_0 f}{U} \tag{19}$$

In the case of the oscillating cylinder, the wake width is also approximated by the amplitude of motion.

4. OSCILLATING CYLINDER IN UNIFORM FLOW

The code was validated using a cylinder in a uniform flow with cross-flow oscillation. This is a well-studied phenomenon and the combination of moving boundary and vortex shedding is very similar to the dynamics observed with flapping hydrofoils. In this section, a comparison

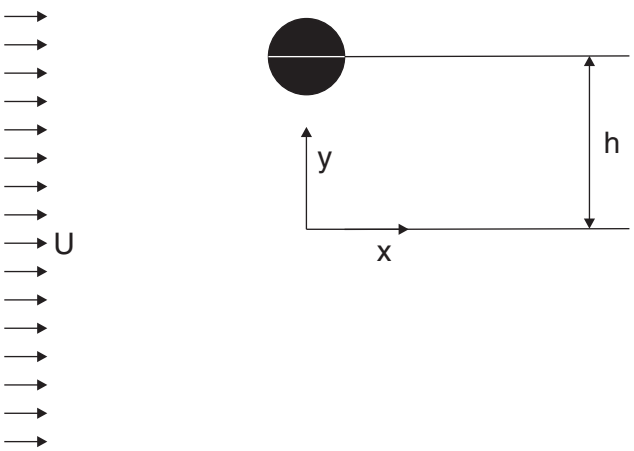

Figure 1. Problem definition of an oscillating cylinder in uniform flow. The distance from the centreline is h.

of the results obtained using CFDLIB with ones obtained in the literature will be made. In particular, the comparison will be made with results obtained by Blackburn and Henderson [20]. This paper was chosen due to the Reynolds number (500) that was used, which is past the transitional Reynolds number of 400 after which the energy transfer phase switch can occur. Also, the authors used a spectral method to solve the flow field. These methods tend to be particularly accurate.

The problem consists of a cylinder of diameter d oscillating in a direction perpendicular (y) to the uniform velocity field direction (x). The study, as in the literature, was performed at a Reynolds number (Ud/v) of 500. One of the most interesting aspects of this kind of oscillation is called the lock-in phenomena. During lock-in, the vortex shedding frequency is the same as the oscillation frequency of the cylinder, therefore, the oscillation drives the vortex shedding. This occurs at oscillation frequencies approximately equal to the shedding frequency of the static cylinder. Simulations were performed with a static cylinder and the Strouhal number was measured to be equal to 0.21.

The relative frequency is defined as

$$F = \frac{f_0}{f_v} \tag{20}$$

where f_0 is the oscillating frequency and f_v is the vortex shedding frequency in the static case. The motion of the cylinder is governed by

$$h(t) = h_{max} \sin(2\pi f_0(t - t_{start})) \tag{21}$$

where h_{max} is the maximum displacement from the centreline and t_{start} is when the oscillation begins (Figure 1).

Lock-in occurs at an interval of F close to 1. For lower amplitudes of oscillation, this interval diminishes. Koopman [22] reported that entrainment (lock-in) can only occur for $h_{max}/d > 0.05$. Therefore, entrainment is assured for a value of $h_{max} = 0.25d$. Another interesting phenomenon is the phase reversal that occurs between $F = 0.90$ and 0.98. The phases

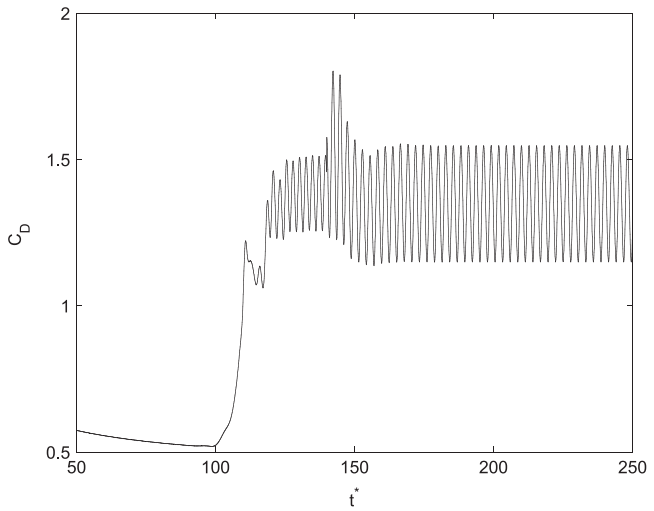

Figure 2. Drag signal for the oscillating cylinder at $F = 0.875$. Cross-flow oscillation commences at $t^* = 140$.

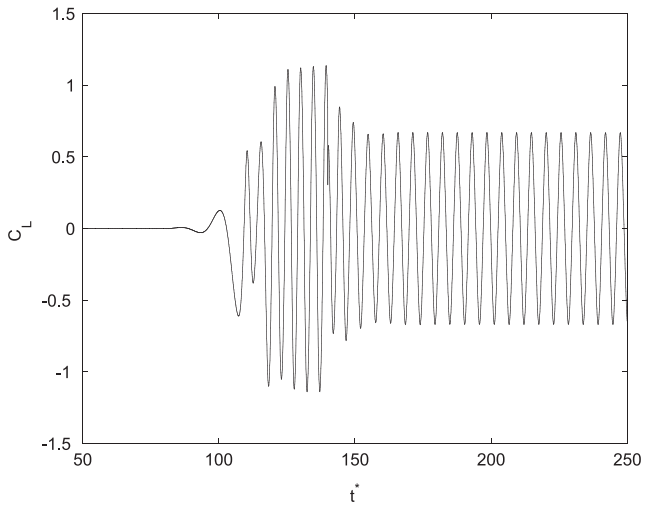

Figure 3. Lift signal for the oscillating cylinder at $F = 0.875$. Cross-flow oscillation commences at $t^* = 140$.

mentioned occur when energy is extracted from the fluid in one phase and added to the fluid in another. This only occurs (as reported by Blackburn and Henderson [20]) for Reynolds numbers above 400; thereby justifying their choice of $Re = 500$. The phase switch is due to different vorticity production mechanisms that are in competition. Along with this phase switch, comes a switch in the sign of energy transfer between fluid and cylinder. As reported by Blackburn and Henderson [20], the transient before lock-in is shorter for oscillation

Table I. Comparison of results with ones obtained by Blackburn and Henderson [20].

	Literature		Present study	
F	$\langle C_d \rangle$	max $\lvert C_l \rvert$	$\langle C_d \rangle$	max $\lvert C_l \rvert$
0.875	1.46	0.72	1.35	0.67

frequencies slightly below the vortex shedding frequency. Therefore, the simulations were run at $F = 0.875$. The drag and lift curves are plotted in Figures 2 and 3. The cylinder was forced to begin oscillating at a non-dimensional time ($t^* = tU/d$) equal to 140. Both the average drag and maximum lift (see Table I) compare favourably with results obtained by Blackburn and Henderson [20]. The streamlines over one cycle are plotted in Figure 4 and shows the formation of the vortices along with the areas of higher fluid velocity which are denoted by the higher density of streamlines.

As can be seen from Figures 2 and 3 the cylinder is kept static until the vortex shedding is stable and is then oscillated. The transient time is relatively short, approximately 30 time units. Also, the lift coefficient is plotted against the cross-flow coefficient in Figure 5.

This plot compares very favourably with the one in Reference [20] for the case $F = 0.875$ and less favourably for $F = 0.975$. This is due to the fact that the phase switch has not yet occurred. The fact that the phase switch has not occurred contradicts Blackburn and Henderson's claims. The difference is that in the present study, the Strouhal number calculated for the static cylinder is too low. Figure 6 highlights the problem. The light grey area denotes the phase where the cylinder transfers energy to the fluid (between $F = 0.98$ and 1.02) while the black area denotes the phase where energy is extracted from the fluid ($F = 0.77$–0.90). The frequencies f_{vB} and f_{vP} are the vortex shedding frequencies calculated for the static cylinder in Reference [20] and in the present study, respectively. As can be clearly seen the shedding frequency calculated in the present study has a smaller value than the one calculated by Blackburn and Henderson. The results obtained in the present study show that in fact, the Strouhal number calculated by Blackburn and Henderson is a better fit in relation to the location of the phases present.

Since the range of frequencies over which the fluid to cylinder energy transfer occurs is quite large in relation to the other phase, it is much easier to obtain favourable simulation results in that range. The other phase presents a greater challenge, as it exists over a small range. This is why the results obtained for $F = 0.875$ are very similar in relation to the results obtained by Blackburn. In the $F = 0.975$, the shedding regime is transitional and therefore a degraded hysteresis curve is developed (Figure 5). In an attempt to reproduce the lock-in at approximately $F = 1$, obtained by Blackburn and Henderson, a simulation was performed at a non-dimensional frequency of 1.05. This would place the Strouhal number at approximately the value obtained by Blackburn and Henderson. The lock-in is never achieved and a quasi-chaotic transient is never surpassed. This transient is very similar to the one obtained by Blackburn and Henderson, with the difference that they achieved a lock-in after approximately 1200 time units.

These results validate the CFD code used and allow for the simulation of more complex geometries, i.e. the flapping hydrofoil.

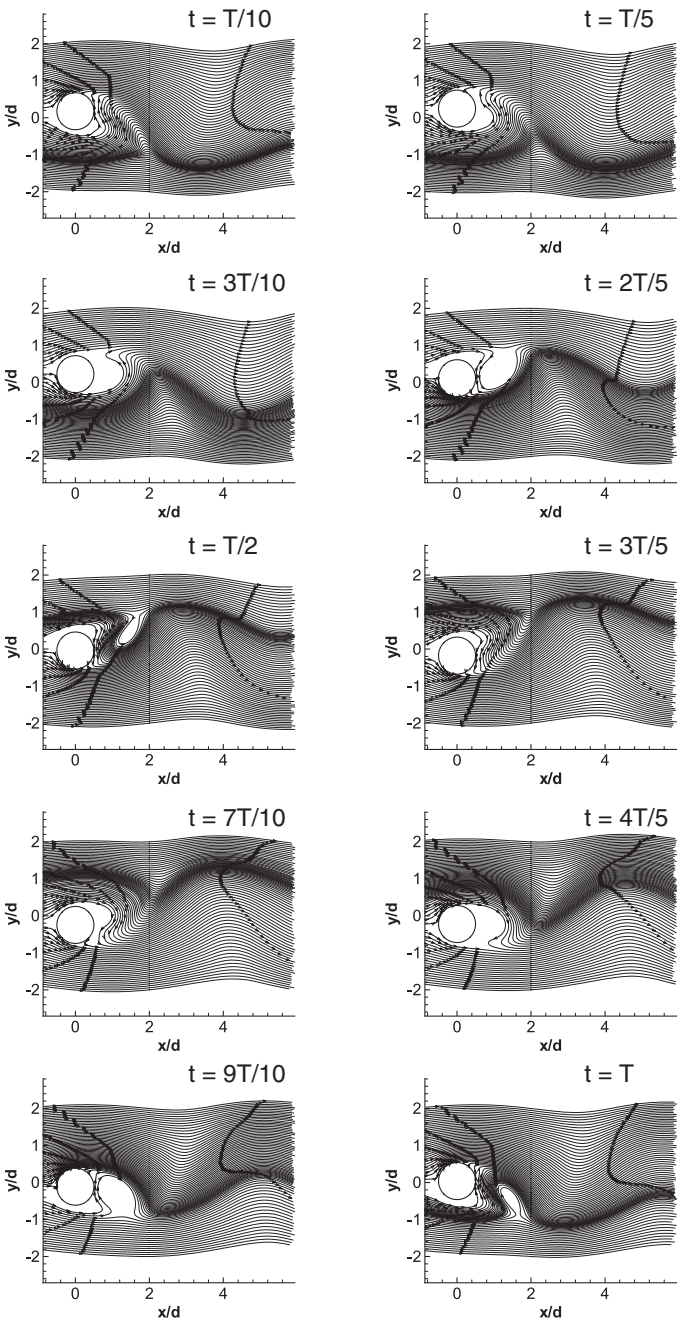

Figure 4. Streamlines for $F = 0.875$ and $Re = 500$ over one cycle.

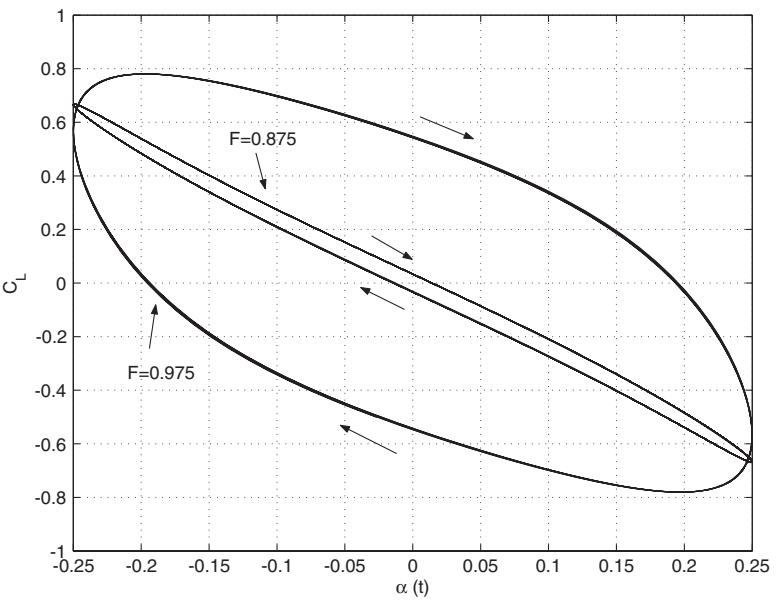

Figure 5. Lift signal versus cross-flow displacement for the oscillating cylinder at $F = 0.875$ and 0.975.

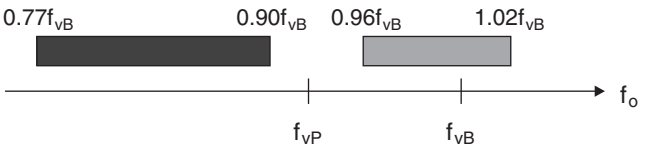

Figure 6. Range of frequencies where the different phases occur for the case of the oscillating cylinder. f_0 is the oscillation frequency, f_{vB} is the shedding frequency for the static cylinder at $Re = 500$ measured by Blackburn and Henderson in Reference [20] and f_{vP} is the shedding frequency for the static cylinder at $Re = 500$ measured in the present study.

5. FLAPPING HYDROFOIL

5.1. Domain

The profile used in this study is a NACA0012 profile. This profile was chosen because it is symmetric, as are caudal fins, and because it is quite slender (maximum thickness is 12% of the chord length, see Figure 8). Also, this profile has been used in various studies and its performance characteristics are well documented in the literature.

The Reynolds number is calculated using the chord length ($Re = Uc/v$) and was set to 1100. The value is low since turbulence models were not used and a direct numerical simulation would be very costly in terms of CPU time. Even though this is a rather low value the results obtained provide excellent insight into the mechanisms of thrust generation.

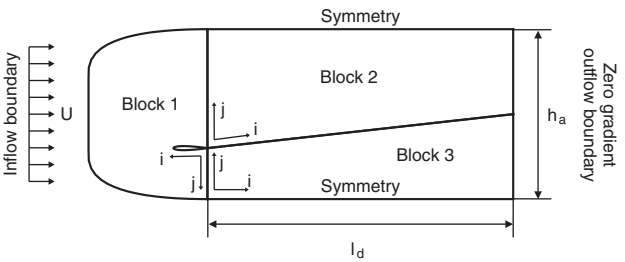

Figure 7. Domain set-up in the case of the hydrofoil.

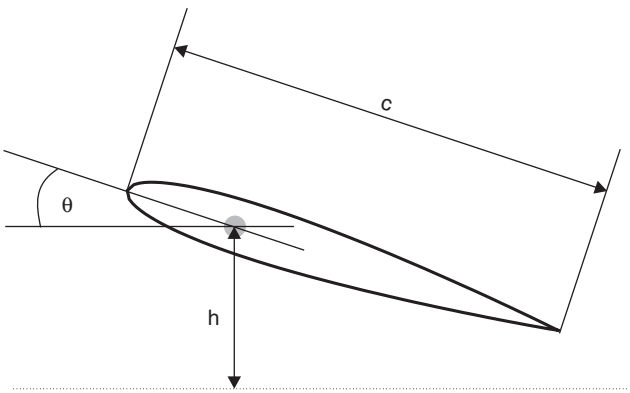

Figure 8. Hydrofoil motion.

The domain is broken up into three blocks. The first is a C-grid around the hydrofoil while the other two are blocks downstream of the hydrofoil. Block 1 has velocity specified boundaries on both the inner (airfoil) and outer surfaces. The outer one is set to a specific free-stream velocity $U = 1$, while on the other boundary corresponding to the airfoil, the fluid velocity is set to a value equal to the surface velocity, making it a wall (no-slip condition). On the downstream blocks (blocks 2 and 3), the top and bottom boundaries are symmetry boundaries while the downstream one is a zero-gradient boundary (see Figure 7).

The only boundaries that move are the hydrofoil and the interface between blocks 2 and 3. After each time step, the grid is re-generated according to the new position and orientation of the hydrofoil. The hydrofoil can pitch (θ) about the z-axis (which is normal to the plane of motion) and heave (h) in the y direction (which is perpendicular to the free stream velocity). The angle of attack (α_a) is the angle between the velocity vector of the hydrofoil and the x-axis. The following equations specify its movement (see Figure 8):

$$h = h_0 \sin[2\pi f(t - t_0) - \Psi] \tag{22}$$

$$\theta = \theta_0 \sin[2\pi f(t - t_0)] \tag{23}$$

where h_0 is the maximum heave amplitude, θ_0 is the maximum pitch angle, f is the oscillation frequency (which is always the same in pitch and heave), t_0 is the time when movement begins and Ψ is the phase difference between pitch and heave (Table II).

Table II. Simulation parameters for the pitching hydrofoil.

#	f (Hz)	k	θ_0 (°)
P1	0.0	0.0	N/A
P2	0.6366	2.0	5
P3	1.2732	4.0	5
P4	1.9098	6.0	5
P5	2.5464	8.0	5
P6	3.1830	10.0	5
P7	3.8196	12.0	5
P8	4.4562	14.0	5
P9	5.0928	16.0	5
P10	5.7294	18.0	5
P11	6.3660	20.0	5

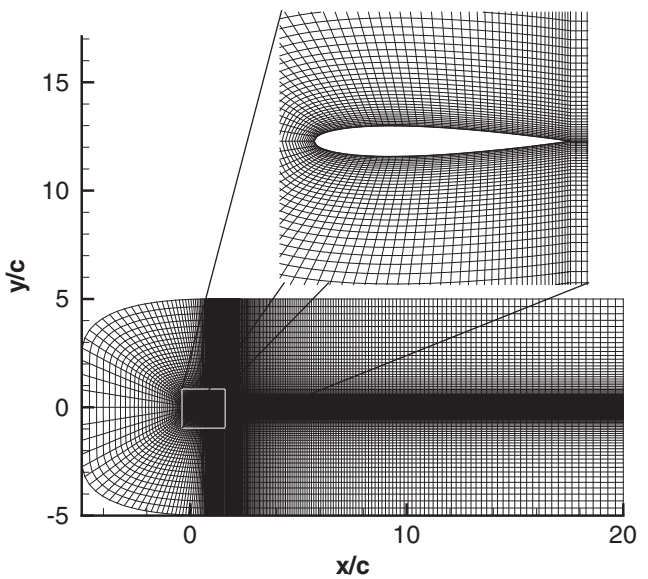

Figure 9. Hydrofoil mesh.

An extensive grid study was undertaken to obtain an optimal grid that could be used in all the simulations. In the end, a hydrofoil mesh consisting of 24 662 cells was used (see Figure 9).

5.2. *Pitching*

In this section, a hydrofoil undergoing a pure pitching motion is studied. There are two variables in this study. The first is the frequency of oscillation (f), which can be expressed through the non-dimensional parameter, the Strouhal number (St), and the second is the maximum pitching angle (θ_0). It is expected that thrust will increase with an increase in

Table III. Simulation results for the pitching hydrofoil.

#	$\overline{C_T}$	$\overline{C_{Tp}}$	$\overline{C_{Tv}}$	$\widehat{C_L}$	$\widehat{C_{Lp}}$	$\widehat{C_{Lv}}$
P1	−0.0581	−0.0175	−0.0405	0.0000	0.0000	0.0000
P2	−0.1132	−0.0276	−0.0857	0.7107	0.7068	0.0039
P3	−0.0904	0.0178	−0.1083	2.3600	2.3478	0.0125
P4	−0.0168	0.1211	−0.1379	5.4341	5.4113	0.0233
P5	0.0964	0.2686	−0.1722	9.8144	9.7787	0.0361
P6	0.2174	0.4322	−0.2147	15.5948	15.5437	0.0518
P7	0.4543	0.7023	−0.2480	23.4162	23.3420	0.0752
P8	0.8624	1.1155	−0.2532	34.1262	34.0215	0.1070
P9	1.2855	1.5596	−0.2740	45.5064	45.3801	0.1299
P10	1.7467	2.0311	−0.2844	57.5248	57.3784	0.1521
P11	2.2184	2.5239	−0.3055	70.6974	70.5301	0.1744

either the maximum pitching angle or the frequency of oscillation. The key question is at what frequency will there be thrust for a certain pitching angle. Summary results are presented and discussed in this section, and detailed simulation parameters along with the results are presented in a tabular format in Table III.

A simulation with a static hydrofoil, with no angle of attack, was initially performed. The drag and lift signals were allowed to converge until no unsteadiness was noticed in either of them. Once the initial transient had died down, the hydrofoil was forced to pitch according to Equation (23). A maximum pitching angle of five degrees was used in all the simulations.

5.3. *Analysis of results*

In this set of simulations, mean positive thrust was achieved at a value of $k = 6.0$ (see Figure 10). The average thrust decreases initially with k before increasing which is to be expected. If the hydrofoil oscillates at a low frequency, the dynamic effects created by this oscillation, namely the injection of momentum, is negligible compared to the drag increase due to the increase in angle of attack. The surface area perpendicular to the flow direction increases, thereby increasing the drag. At a certain value of k ($k = 2$ in this case) the drag starts to decrease as the higher frequency of oscillation begins to inject more momentum into the flow, as was also verified by Koochesfahani [12]. At values above $k = 6.0$ thrust is created but the viscous component still has an average value below zero, though. Therefore, the viscous component is reducing the thrust (adding drag). This is to be expected as the viscous component is based on the shear stresses on the hydrofoil surface. These shear stresses, in a static hydrofoil with no separation, always have a direction towards the trailing edge, thereby increasing the drag. In the pitching airfoil, except where there is vortex shedding, the shear stresses maintain this general direction, thereby reducing the thrust. This is expected at all frequencies.

5.4. *Flow field visualization*

An analysis of the flow field in this kind of simulation is crucial in the understanding of the vortical pattern created by the oscillating hydrofoil which is responsible for elevated drag in certain cases, but also thrust in others.

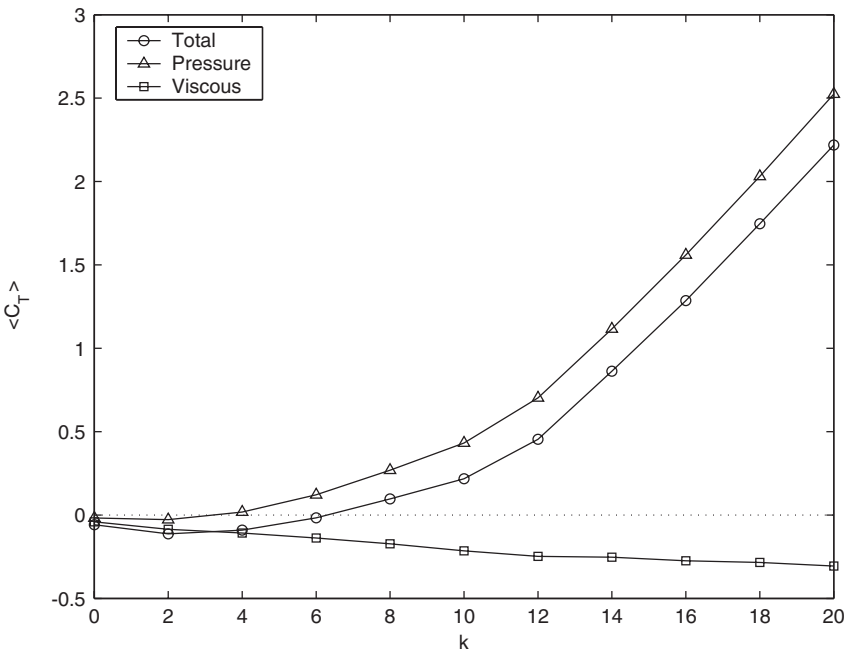

Figure 10. Average thrust versus wave number for a pitching airfoil with a maximum pitch angle of 5°.

Figure 11 shows a contour plot of vorticity over one cycle of oscillation for case P5, where thrust is generated. Blue denotes negative vorticity (fluid is rotating in a clockwise direction) while red denotes positive vorticity (fluid rotates in a counter clockwise direction).

In Figure 11a reverse Kármán vortex street is present. This indicates a jet flow which is responsible for the thrust that is generated. During each cycle two vortices are created: a top one and a bottom one. The generation of these vortices is identical in everything but the direction. Therefore, in analysing the generation of one of the vortices being shed, the full mechanism can be understood:

- $t = T/4$: The trailing edge is at its lowest position, and is at rest. No vorticity is evident near the hydrofoil surface.
- $t = 3T/8$: The trailing edge starts to rise. The fluid is no longer at rest near the surface. The fluid below the hydrofoil is dragged along while the fluid on the top surface is accelerated downstream. The fluid above the hydrofoil is injected in a jet like manner out the top and is forced down by the vorticity created by the fluid below the hydrofoil that is being dragged.
- $t = T/2$: The trailing edge is moving its maximum velocity in the cycle as it passes zero angle of attack. The vortex has increased in strength and size but is still attached to the hydrofoil.
- $t = 5T/8$: The trailing edge starts to slow down and the vortex is shed.
- $t = 3T/4$: The trailing edge is at its highest position. The cycle begins again, but in the next half cycle a vortex that rotates in the counter clockwise direction is shed.

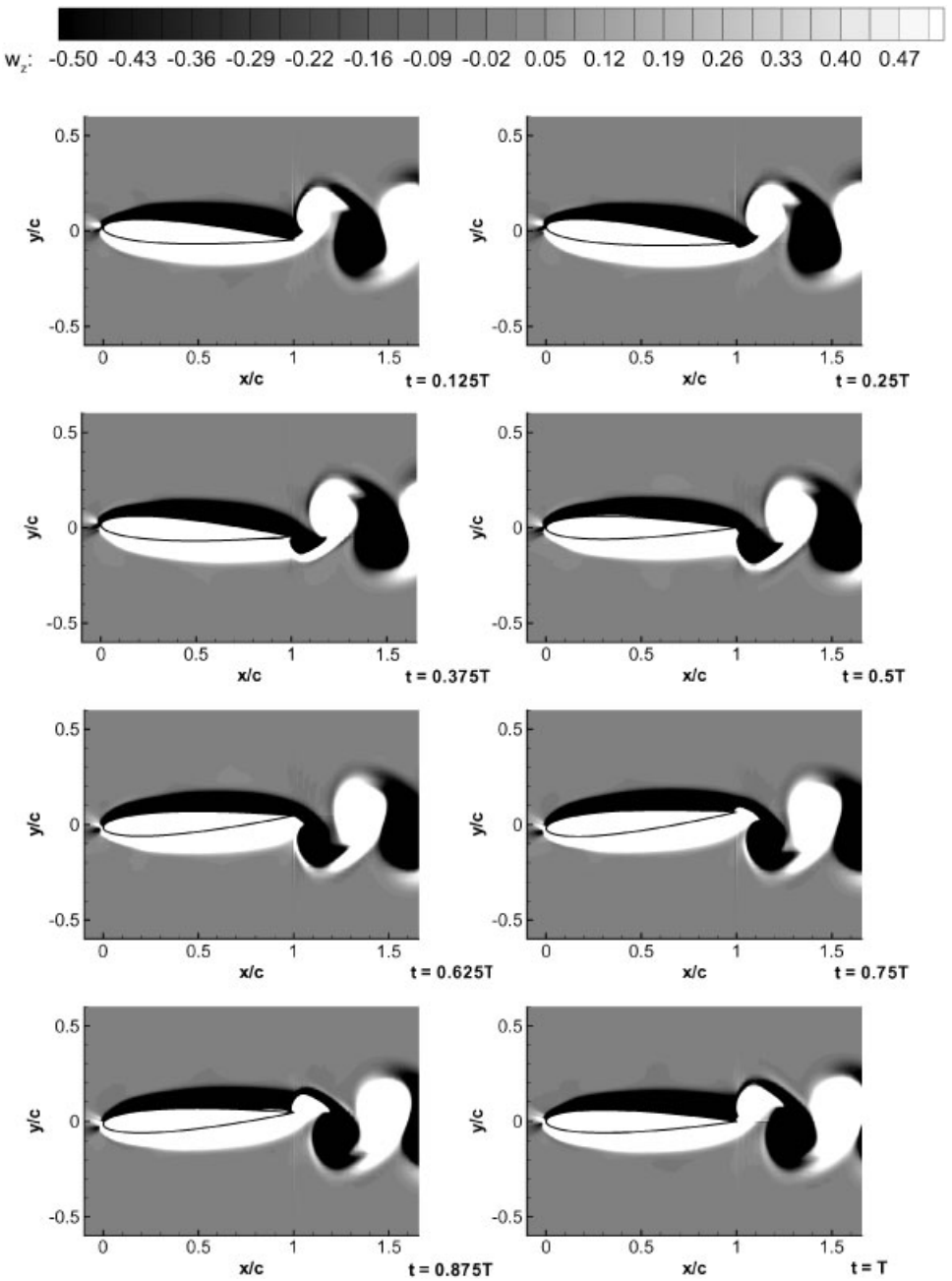

Figure 11. Vorticity contours over one cycle $k = 8$.

Table IV. Simulation parameters for the pitching and heaving hydrofoil.

#	f (Hz)	h_0/c	θ_0 (°)	Ψ (°)	k	St	α_a (°)
T1	0.225	1.0	5	90	0.7096	0.45	49.45
T2	0.225	1.0	10	90	0.7096	0.45	44.51
T3	0.225	1.0	15	90	0.7096	0.45	39.58
T4	0.225	1.0	20	90	0.7096	0.45	34.64
T5	0.225	1.0	25	90	0.7096	0.45	29.70
T6	0.225	1.0	30	90	0.7096	0.45	24.76
T7	0.225	1.0	40	90	0.7096	0.45	14.88
T8	0.225	1.0	50	90	0.7096	0.45	5.01
F1	0.050	1.0	30	90	0.1571	0.10	−12.56
F2	0.100	1.0	30	90	0.3142	0.20	2.14
F3	0.150	1.0	30	90	0.4712	0.30	13.30
F4	0.200	1.0	30	90	0.6283	0.40	21.49
F5	0.250	1.0	30	90	0.7854	0.50	27.52
F6	0.300	1.0	30	90	0.9425	0.60	32.05
F7	0.350	1.0	30	90	1.0996	0.70	35.55
F8	0.400	1.0	30	90	1.2566	0.80	38.30
F9	0.500	1.0	30	90	1.5708	1.00	42.34
PS1	0.250	0.5	30	30	0.7854	0.50	−8.56
PS2	0.250	0.5	30	50	0.7854	0.50	1.03
PS3	0.250	0.5	30	70	0.7854	0.50	6.43
PS4	0.250	0.5	30	90	0.7854	0.50	8.15
PS5	0.250	0.5	30	100	0.7854	0.50	7.72
PS6	0.250	0.5	30	105	0.7854	0.50	7.19
PS7	0.250	0.5	30	110	0.7854	0.50	6.43
PS8	0.250	0.5	30	115	0.7854	0.50	5.44
FIN1	0.200	0.5	40	100	0.6283	0.200	−8.25
FIN2	0.250	0.5	40	100	0.7854	0.250	−2.28
FIN3	0.275	0.5	40	100	0.8639	0.275	0.39
FIN4	0.300	0.5	40	100	0.9425	0.300	2.87
FIN5	0.325	0.5	40	100	1.0210	0.325	5.16
FIN6	0.350	0.5	40	100	1.0996	0.350	7.28
FIN7	0.375	0.5	40	100	1.1781	0.375	9.24

The pitching motion of a hydrofoil provides insight into the generation of thrust using vorticity control. The mechanism is essentially the same, whether one is pitching the airfoil or combining this motion with heaving. Obviously, while the mechanism is practically the same, the thrust, lift and moment produced are radically different which in turn impacts on the power and efficiency of this type of motion. In the next section, the hydrofoil is pitched and heaved in an effort to discover a superior form of thrust generation (Table IV).

5.5. Combined pitching and heaving

This section is devoted to the study of the hydrofoil that is not only pitching but also heaving at the same time. The goal is to study the effect that the motion variables have on the values

Table V. Simulation results for the pitching and heaving hydrofoil.

#	$\overline{C_{\mathrm{T}}}$	$\overline{C_{\mathrm{T}p}}$	$\overline{C_{\mathrm{T}v}}$	$\widehat{C_{\mathrm{L}}}$	$\widehat{C_{\mathrm{L}p}}$	$\widehat{C_{\mathrm{L}v}}$	$\widehat{C_M}$	$\overline{C_{\mathrm{P}}}$	η
T1	0.4324	0.4429	−0.0105	8.3333	8.2620	0.0729	0.80	4.75	0.09
T2	0.6511	0.6651	−0.0140	7.4834	7.4127	0.0744	0.68	4.24	0.16
T3	0.8226	0.8408	−0.0183	6.6307	6.5607	0.0764	0.58	3.78	0.22
T4	0.9337	0.9584	−0.0246	5.8176	5.7493	0.0833	0.51	3.31	0.28
T5	1.0046	1.0387	−0.0341	5.0558	4.9908	0.0960	0.45	2.88	0.35
T6	1.0166	1.0601	−0.0435	4.3721	4.3132	0.1117	0.41	2.40	0.42
T7	0.7404	0.8102	−0.0697	3.2278	3.1603	0.1442	0.48	1.34	0.55
T8	0.2953	0.4084	−0.1131	2.7345	2.6602	0.1532	0.55	0.53	0.56
F1	−0.2524	−0.1807	−0.0717	0.7626	0.7705	0.0238	0.04	−0.08	—
F2	−0.0705	0.0155	−0.0860	0.4395	0.4079	0.0517	0.01	0.08	—
F3	0.3509	0.4232	−0.0723	1.6402	1.5860	0.0743	0.08	0.75	0.47
F4	0.7886	0.8373	−0.0488	3.3332	3.2825	0.0989	0.14	1.74	0.45
F5	1.3377	1.3770	−0.0392	5.5198	5.4515	0.1257	0.16	3.47	0.39
F6	1.9968	2.0283	−0.0315	8.1910	8.1015	0.1537	0.88	6.05	0.33
F7	2.9075	2.9291	−0.0216	11.8457	11.7333	0.1802	1.34	10.18	0.29
PS1	−0.2463	−0.2334	−0.0129	2.0587	2.0148	0.0451	0.26	0.31	—
PS2	−0.0541	−0.0188	−0.0352	1.4769	1.4462	0.0393	0.23	0.23	—
PS3	0.0668	0.1422	−0.0754	0.6438	0.6079	0.0564	0.07	0.29	0.23
PS4	0.0970	0.1949	−0.0979	1.3069	1.2608	0.0718	0.22	0.30	0.32
PS5	0.1448	0.2454	−0.1006	1.9518	1.9024	0.0745	0.30	0.43	0.34
PS6	0.1681	0.2665	−0.0984	2.3054	2.2544	0.0753	0.35	0.50	0.34
PS7	0.1868	0.2806	−0.0937	2.6738	2.6215	0.0759	0.40	0.57	0.33
PS8	0.1937	0.2812	−0.0874	3.0684	3.0150	0.0768	0.41	0.65	0.30
FIN1	−0.2960	−0.2110	−0.0850	1.7271	1.7224	0.0340	0.33	−0.19	—
FIN2	−0.0993	0.0074	−0.1066	2.4923	2.4578	0.0631	0.54	−0.03	—
FIN3	−0.0912	0.0251	−0.1163	2.9705	2.9238	0.0786	0.66	−0.01	—
FIN4	0.0130	0.1384	−0.1253	3.5179	3.4596	0.0948	0.80	0.11	0.12
FIN5	0.1676	0.3012	−0.1336	4.1444	4.0746	0.1117	0.96	0.30	0.56
FIN6	0.3529	0.4939	−0.1411	4.8575	4.7765	0.1293	1.14	0.55	0.64
FIN7	0.5058	0.6539	−0.1480	5.6641	5.5721	0.1473	1.34	0.79	0.64

of thrust, lift, power and efficiency. Once again the results are presented in tabular form in Table V.

Table IV contains the values given to each of the variables for all the pitch and heave simulations. There are three series of simulations which are geared to study the evolution of the parameters as one changes a particular variable. The fourth and final set of simulations is focused upon providing the most efficient form of propulsion over a range of oscillation frequencies.

Before embarking on a parametric study, an analysis of the thrust and lift over one period of oscillation will help in better understanding the problem. Figure 12 shows the lift and thrust signals over one period of time as well as the pitch and heave curves of the same period. One period consists of an up- and a down-strokes. In this case, the pitch and heave have a phase difference of 90°. The maximum heave is of one chord length while the maximum pitch is 30°. Since the up- and down-strokes are symmetrical, the thrust signal has double the

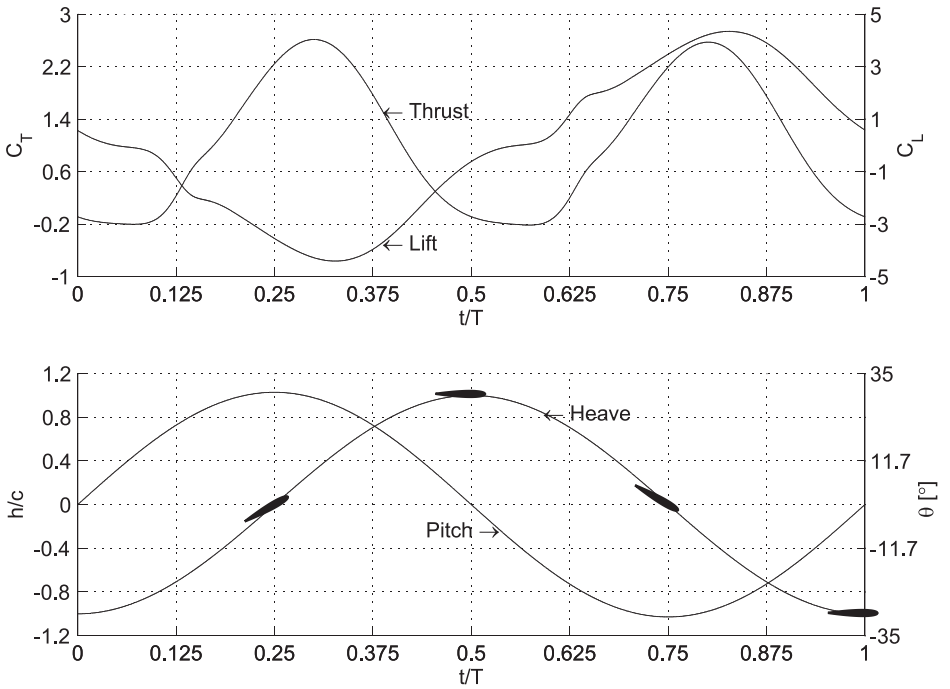

Figure 12. The top figure shows the evolution of the thrust and lift coefficients in time over one period of oscillation while the bottom one shows the variation of the pitch and heave over the period, essentially tracking the movement of the hydrofoil. The hydrofoil profile is not to scale.

frequency of the lift signal. The lift signal's fundamental frequency component is equal to the pitch and heave signal frequency. On the up-stroke a high pressure zone is created on the hydrofoil's top surface and a low pressure zone is created on the bottom surface. This gives a lift force with a downwards direction. Since the airfoil has a positive pitch angle (nose up), the force created by the pressure differential is inclined forward, thereby resulting in thrust. As the hydrofoil is moving from one extreme (in heave) to another, it reaches its maximum heave velocity at the centreline ($h/c = 0$). In fact, the heaving velocity changes very little between approximately $0.1T$ and $0.4T$ (and between $0.6T$ and $0.9T$). At $0.4T$ (and $0.9T$), the hydrofoil starts to slow noticeably and that is when the vortex is shed. At the maximum heave, the hydrofoil inverts its direction of motion and starts to plunge in the other direction. At this point lift is zero as the hydrofoil is at zero angle of attack.

5.5.1. Effect of maximum pitching angle (θ_0). The first study is to determine the best maximum pitch angle. This will determine the angle at which the hydrofoil cuts through the water. The maximum pitch angle (θ_0) is varied from 5 to 50° as the rest of the variables (f, h_0/c and Ψ) are kept constant.

Figure 13 shows the average thrust coefficient as one varies the maximum pitch angle. There is a maximum at approximately 30° for both the total thrust and the pressure component of the thrust. The viscous component reduces, thereby increasing the drag. Looking at the plot of

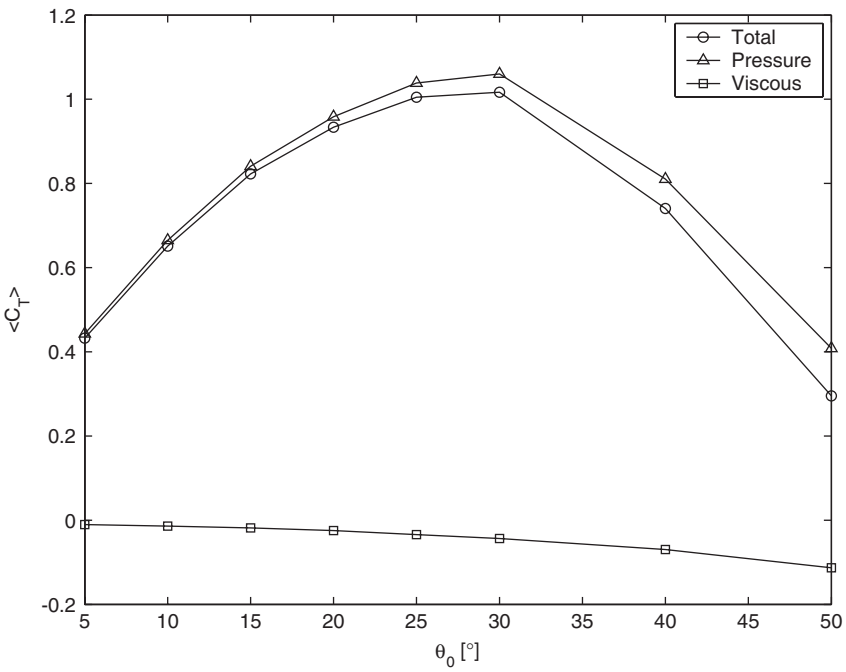

Figure 13. Average thrust coefficient versus maximum pitching angle; $h_0/c = 1.0$, $\Psi = 90°$, $St_h = 0.225$.

maximum lift versus maximum pitch angle (Figure 14), the maximum lift coefficient decreases with increasing θ_0. The maximum moment has a minimum at an angle of 30°, while the power decreases linearly with an increase in θ_0. The efficiency increases to a maximum value of 54% at an angle of 50°.

The thrust generation mechanism is the same as the one described for the pure pitching motion: momentum is added to the flow field by accelerating the fluid around the hydrofoil. At low pitching angles, little fluid is accelerated downstream. Rather, the motion of the hydrofoil displaces the water in a predominantly vertical direction and since the hydrofoil is sloped, the fluid is accelerated downstream. The higher the pitching angle, the more the fluid is accelerated downstream. The pressure difference between the bottom and top surfaces of the hydrofoil, which in turn creates the thrust and lift, changes direction as one increases the pitch angle. The angle between this force vector and the x direction decreases as one increases θ_0. Therefore the thrust coefficient increases as one increases θ_0 while the lift signal decreases.

If one angles the hydrofoil such that the pitch angle of the hydrofoil equals the angle that the path of the heaving motion follows, i.e. maximum value of 54°, or close to this value, the hydrofoil attains maximum efficiency. This is because the lift amplitude is minimized, as is the power (Equation (13)), thereby maximizing the efficiency. The hydrofoil 'snakes' its way through the fluid, displacing less in the horizontal and vertical directions, thereby decreasing the thrust and lift. The reduction in thrust is less than the reduction in power (which depends heavily on lift), thereby resulting in an increase in efficiency. This can be easily verified by noting that, as one increases the pitch angle, the angle of attack decreases,

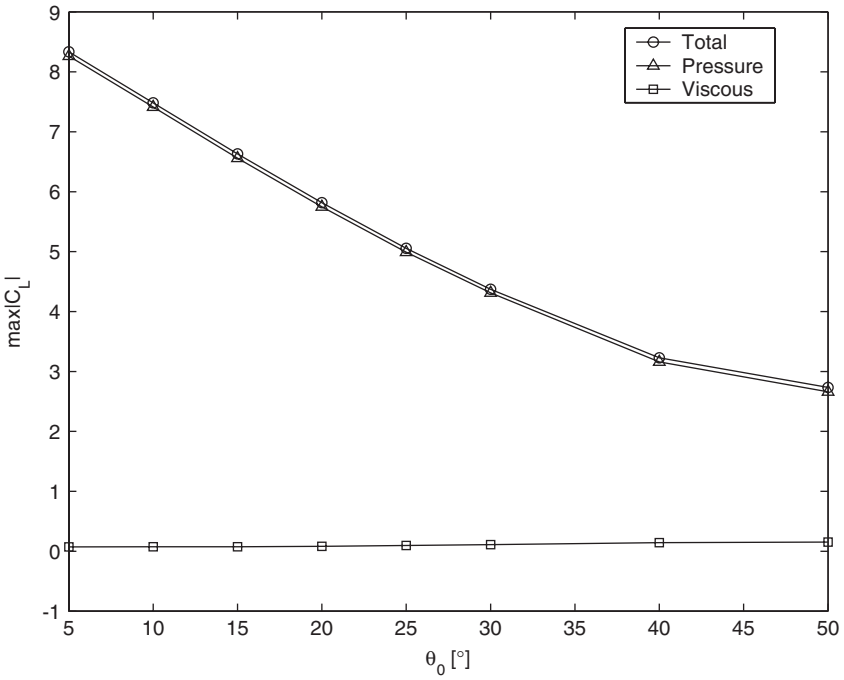

Figure 14. Maximum lift versus maximum pitching angle; $h_0/c = 1.0$, $\Psi = 90°$, $St_h = 0.225$.

reaching a maximum value of 5° when the maximum pitch angle is at 50°. This supports the previous argument (Figures 15 and 16).

To choose a point of operation, one has to balance the need for greater thrust without sacrificing efficiency. Maximum efficiency is obtained above 30° while the thrust generated is reduced. Therefore, a maximum pitching angle of 30° seems optimal.

Figures 17 and 18 compare the vorticity fields of three simulations over half a cycle of oscillation. Frames (a) through (e) in Figure 17 shows the vortex shedding in the case where $\theta_0 = 30°$ (T6) while frames (f) to (h) is when $\theta_0 = 5°$ (T1). Both the average thrust and efficiency are higher for simulation T6 (see Figures 13 and 16). The higher pitch angle generates smaller, more compact vortices while a lower pitch angle tends to create less coherent vortices as can be seen if one compares frames (d) and (h). In the latter frame, the main vortex (rotating in a counter clockwise direction) is paired with a smaller vortex rotating in the opposite direction, which results in a loss of efficiency. Also the shape of the vortex is less well defined and larger than the one in frame (d).

Increasing θ_0 beyond 30° increases the efficiency but results in a decrease in the thrust generated. Frames (a) through (d) once again show the case where $\theta_0 = 30°$ while frames (e) through (h) show the case where $\theta_0 = 50°$. In frames (e)–(h) the vortices created are smaller and spread out more. The power required to create the vortex is lower as is the thrust generated.

Figure 19 shows the generation of a vortex near the hydrofoil surface for simulations T3 (a), T1 (b) and T8 (c). As the maximum pitching angle is increased, the vortex size

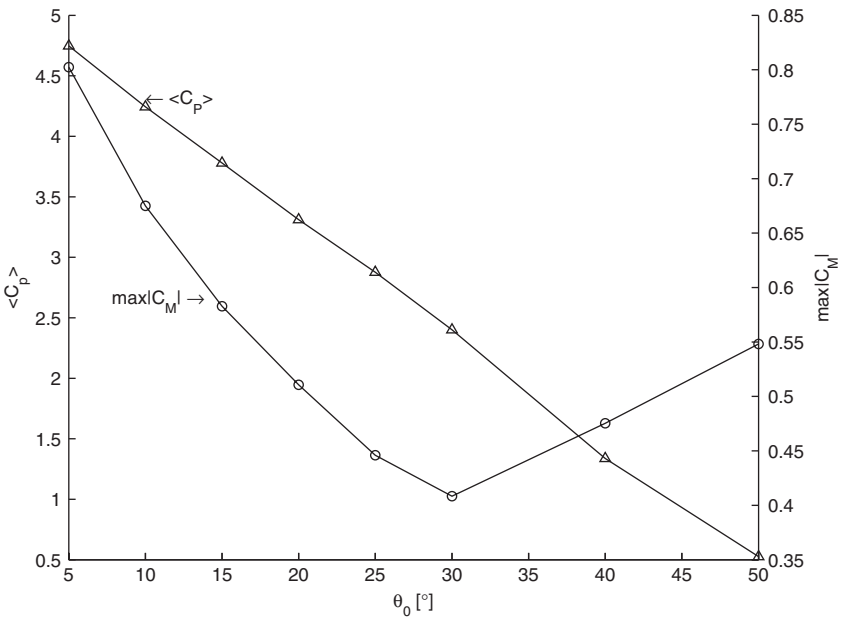

Figure 15. Average power and maximum moment coefficients versus maximum pitching angle; $h_0/c = 1.0$, $\Psi = 90°$, $St_h = 0.225$.

decreases. In frame (c) the separation occurs much closer to the trailing edge than for the other two cases. Also, a secondary vortex is created in case T1 which is closer to the leading edge and which does not exist in the other two cases. The further back a vortex is generated, the more compact it will be. Also, secondary vortices tend to increase the power requirements while not necessarily increasing the thrust. Next, the effect of the Strouhal number is studied in greater detail.

5.5.2. Effect of Strouhal number (St). Strouhal number is a crucial parameter in the thrust generation mechanism. Also, as will be described in this section, a small change in frequency can alter quite significantly thrust and efficiency.

This is emphasized in Figures 20 and 21. From Figure 20 one can see that thrust is positive for Strouhal numbers above 0.2, and it increases as one increases the Strouhal number. Efficiency reaches a maximum very quickly as one increases St. If one neglects viscous effects, efficiency is maximized as average thrust reaches 0. This is equivalent to saying that a craft operating in an ideal fluid requires no thrust, or power to travel at a certain velocity. At this point energy is neither drawn nor supplied, which is unphysical. By introducing viscosity it is evident that power will always be required to overcome viscous forces. The total average thrust needed is again 0, but the efficiency can never be 100%. Based on the present study, maximum efficiency is achieved at a Strouhal number slightly above the one required to produce thrust.

The Strouhal numbers were limited to a maximum of 0.7 in this set of simulations as the trend does not change once maximum efficiency has been reached.

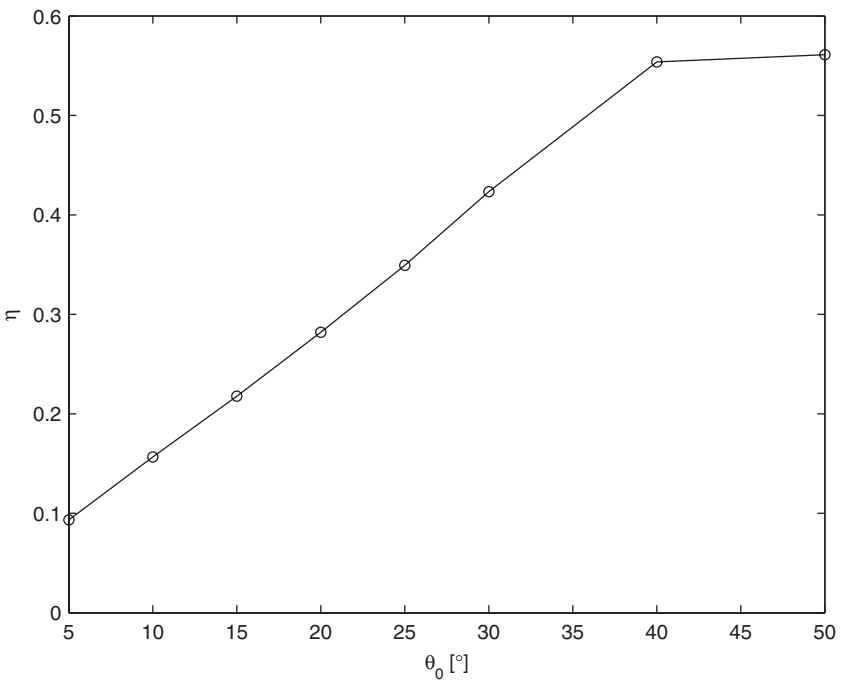

Figure 16. Efficiency versus maximum pitching angle; $h_0/c = 1.0$, $\Psi = 90°$, $St_h = 0.225$.

The increase in average thrust, maximum lift and average power can be attributed to the higher relative velocity of the hydrofoil as the Strouhal number increases. The pressure differences increase thereby resulting in higher lift and thrust.

While a change in Strouhal number has a predictable effect on the parameters, the effect of phase angle on the parameters is not as straightforward.

5.5.3. Effect of phase angle (Ψ). In most of the simulations in this chapter the heaving and pitching motion are out of phase by $\Psi = 90°$. This section studies the effect of varying this angle. Eight simulations were run to study the effect that varying Ψ from 30 to 115° would have on the average thrust coefficient (see Figure 22) and efficiency (see Figure 23).

Varying the phase from 90° causes the hydrofoil to have a non-zero pitch angle at the top and bottom positions. If the phase angle is greater than 90°, at the lowest position of the heaving motion the hydrofoil will pitch upwards, while if the phase angle is less than 90°, at the same position, the hydrofoil will pitch down.

The average thrust coefficient increases with Ψ. Below 60° the average thrust is negative, or rather drag is created. At very low phase angles the hydrofoil is almost paddling backwards, countering the free stream instead of swimming with it, thereby explaining the drag. The maximum lift coefficient has a minimum at 70° and then increases rapidly. Simulation PSI3 ($\Psi = 70°$) has the lowest value of Ψ where the thrust is positive. The hydrofoil starts to produce thrust at some point between these two values.

Power increases with phase for angles greater than 70°. This is to be expected as the greatest contributor to power is lift, i.e. as the maximum lift increases, so does the power.

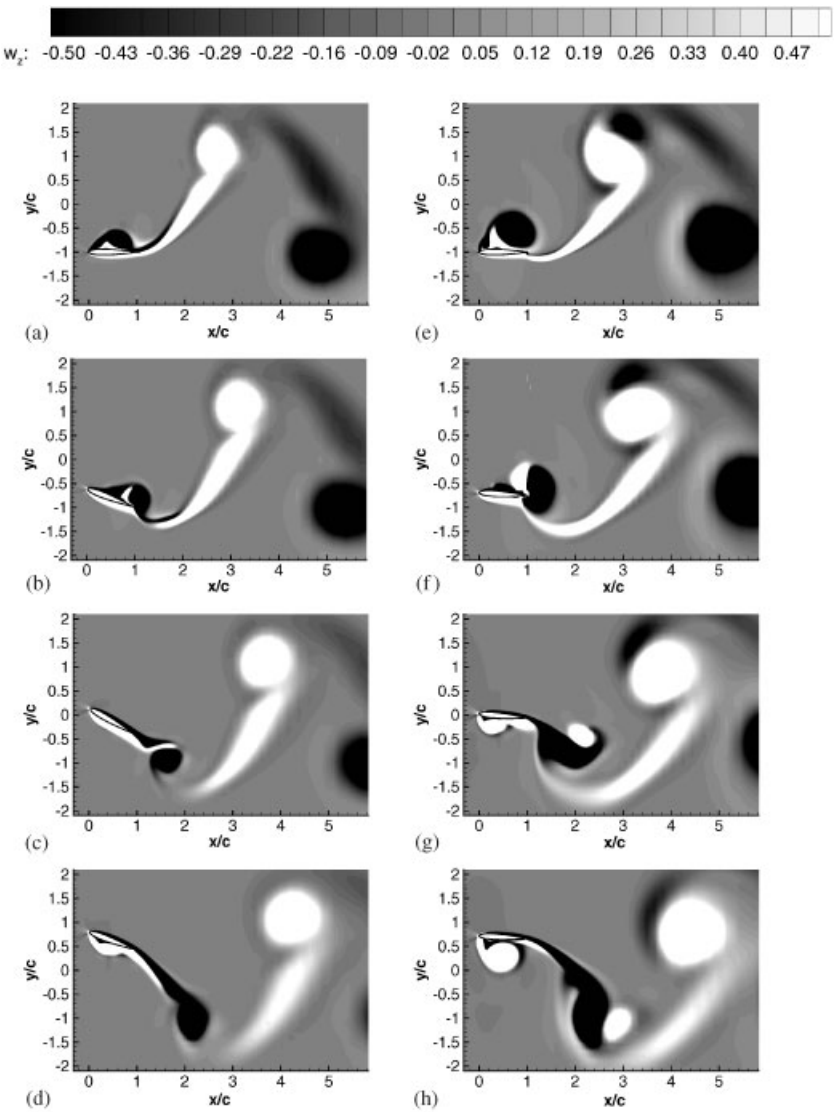

Figure 17. Vorticity plot over half a cycle (snapshots at $t = 0$, $0.125T$, $0.25T$ and $0.375T$) for cases T6 (a)–(d) and T1 (e)–(h). In T6, the maximum pitching angle is 30°, while in T1 the maximum pitching angle is 5°.

Moment reaches its minimum at 70° and increases after that. Efficiency is only of interest if thrust is being produced, as this is the regime in which one wishes to operate. Above 60° the efficiency varies from 0 to 34% with the maximum value occurring at $\Psi = 100°$. To better understand why this occurs, the flow field must be analysed.

For flow field comparison the base case was chosen to be PSI4, as a phase angle of 90° is an obvious middle value. Cases PSI3 ($\Psi = 70°$) and PSI7 ($\Psi = 110°$) were compared to this

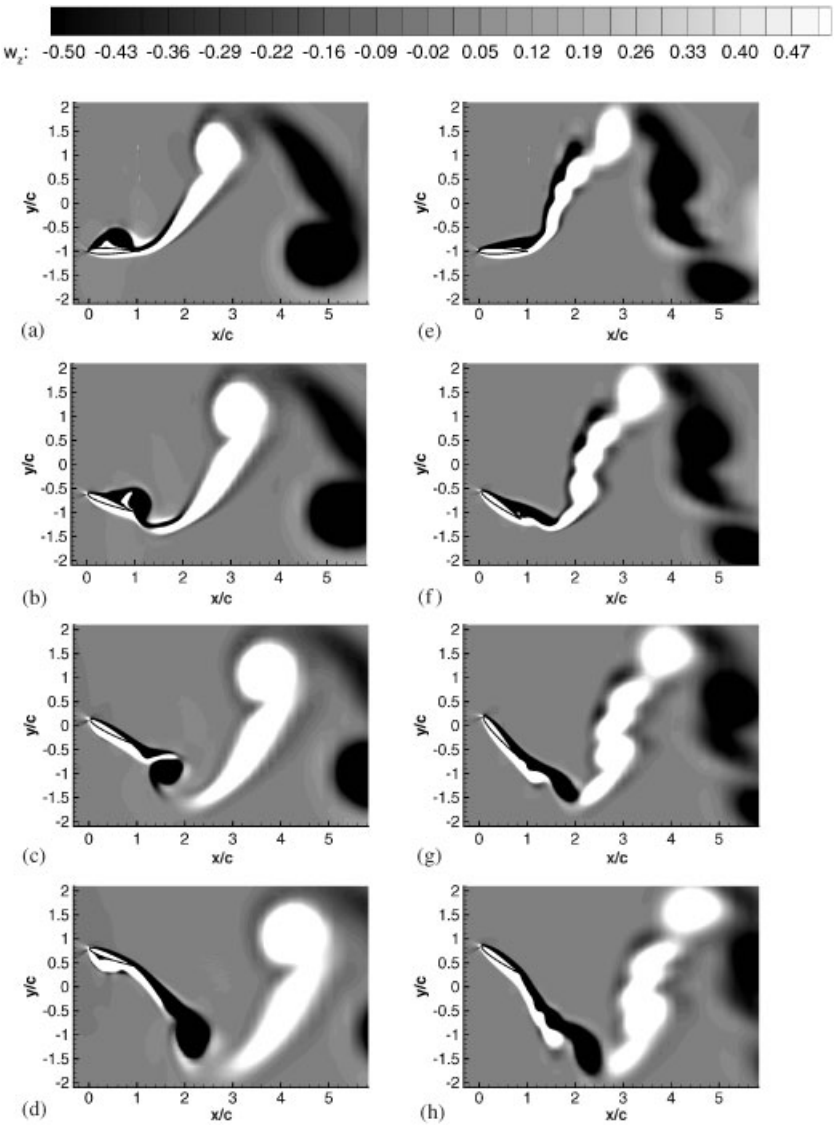

Figure 18. Vorticity plot over half a cycle (snapshots at $t = 0$, $0.125T$, $0.25T$ and $0.375T$) for cases T6 (a)–(d) and T8 (e)–(h). In T6, the maximum pitching angle is 30°, while in T8 the maximum pitching angle is 50°.

base case. The thrust signal in time, of simulation PSI3 are compared with the ones in PSI4 in Figure 24. The signals for simulation PSI3 (frame (b) in all the aforementioned plots) are quite different from the ones for higher phase angles. The peak values are lower in value, but seem to hold the same level for a large amount of time. These distortions occurs at mid heave ($h \approx 0$) where all the coefficients except moment reach their maximum.

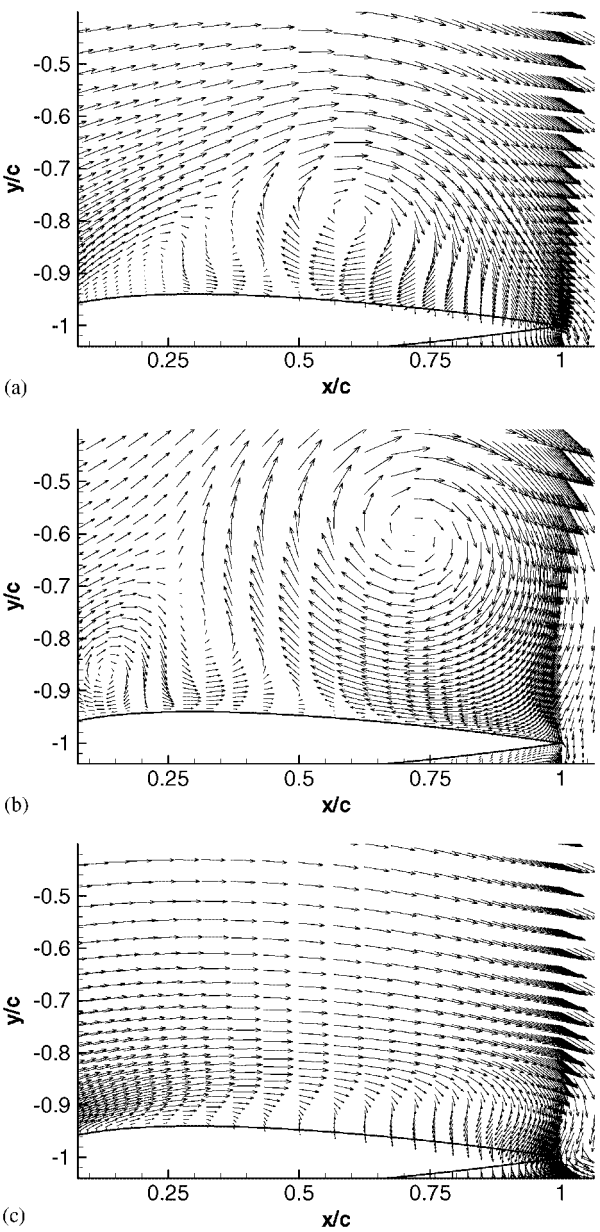

Figure 19. Velocity field at the beginning of a new cycle, i.e. hydrofoil is at its lowest position ($t = 0$): (a) simulation T6 where $\theta_0 = 30°$; (b) simulation T1 where $\theta_0 = 5°$; (c) simulation T8 where $\theta_0 = 50°$.

To find some explanation for this, attention turns to Figure 25 where the vorticity over half a cycle is plotted for both PSI3 and PSI4. In the case where $\Psi = 70°$ (frames (e)–(h)), a strong vortex rotating in the opposite direction to the main vortex is found very close to the main vortex. This accounts for the lower efficiency and thrust in simulation PSI3. Energy is

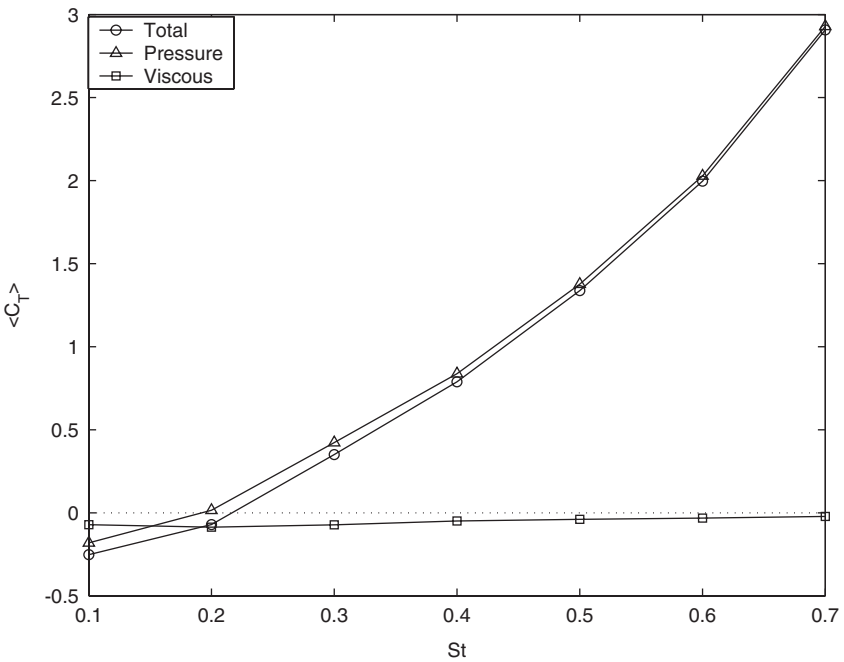

Figure 20. Average thrust coefficient versus Strouhal number; $\theta_0 = 30^\circ$ $h_0/c = 1.0$, $\Psi = 90^\circ$.

lost generating this vortex which is not as strong in the case where $\Psi = 90^\circ$ (frames (a)–(d)). Also, in frames (e)–(h) this vortex induces a break-up of the main vortex into two separate parts; a phenomenon which does not occur in frames (a)–(d).

5.6. *Maximizing efficiency*

One can synthesize the findings from the previous sets of simulations and attempt a series of simulations that will maximize efficiency. In this section, the results obtained from just such a set (FIN) is analysed.

In order to maximize efficiency, the motion variables were set to the following values:

- Maximum pitch angle, $\theta_0 = 40^\circ$,
- phase angle, $\Psi = 100^\circ$ and
- heaving amplitude $h_0/c = 0.5$.

The Strouhal number was altered by changing the frequency of oscillation. The performance of the hydrofoil was studied for Strouhal numbers ranging from 0.2 to 0.375. The maximum efficiency was expected to fall somewhere in this range, as was shown by previous simulations. The average thrust coefficient increased with the Strouhal number and is positive for Strouhal numbers above 0.3 (see Figure 26). Efficiency is maximized at a Strouhal number of approximately 0.35 (see Figure 27), at a value of 64%. This is well above the results obtained in previous simulations.

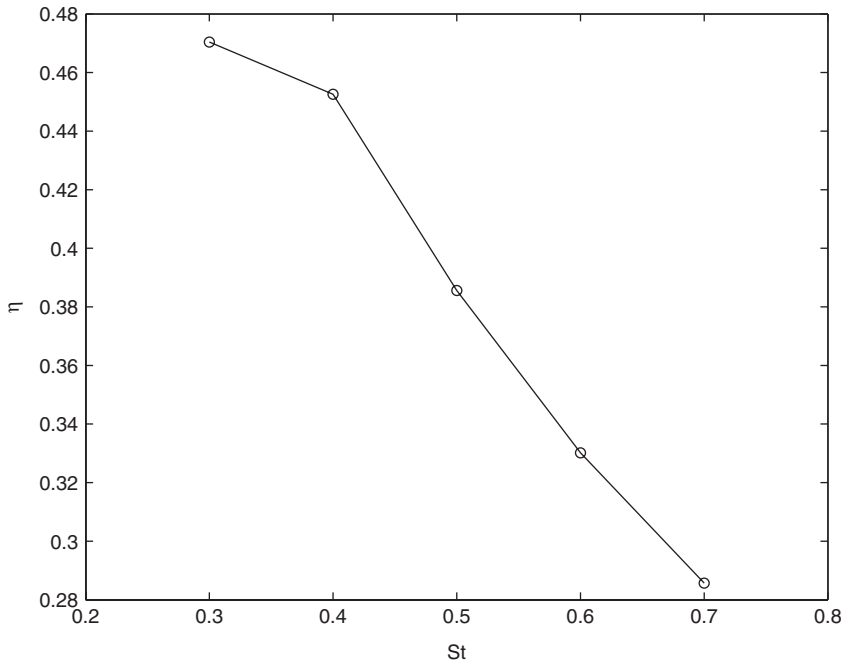

Figure 21. Efficiency versus Strouhal number; $\theta_0 = 30^\circ$ $h_0/c = 1.0$, $\Psi = 90^\circ$.

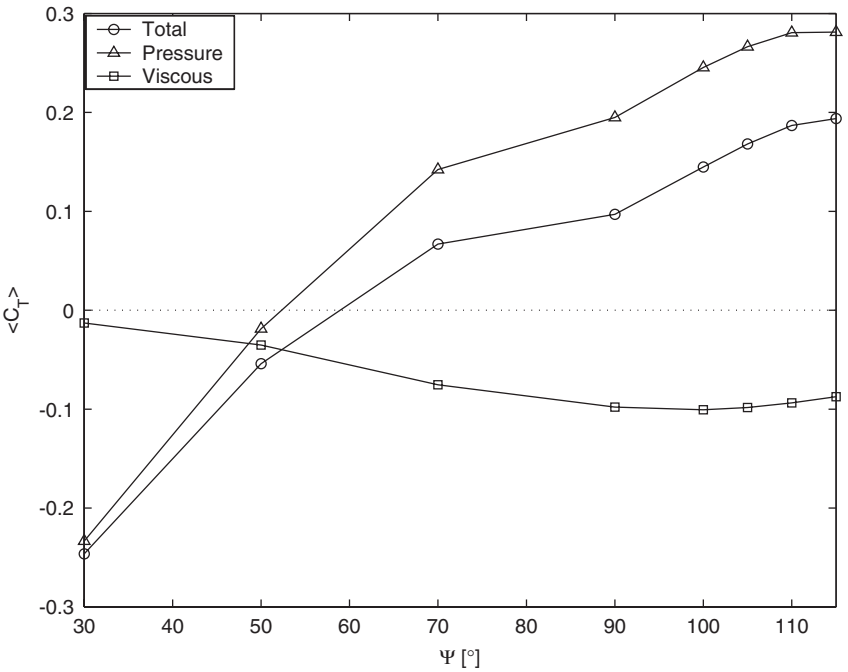

Figure 22. Average thrust coefficient versus phase angle; $h_0/c = 0.5$, $\theta_0 = 30^\circ$, $St_h = 0.25$.

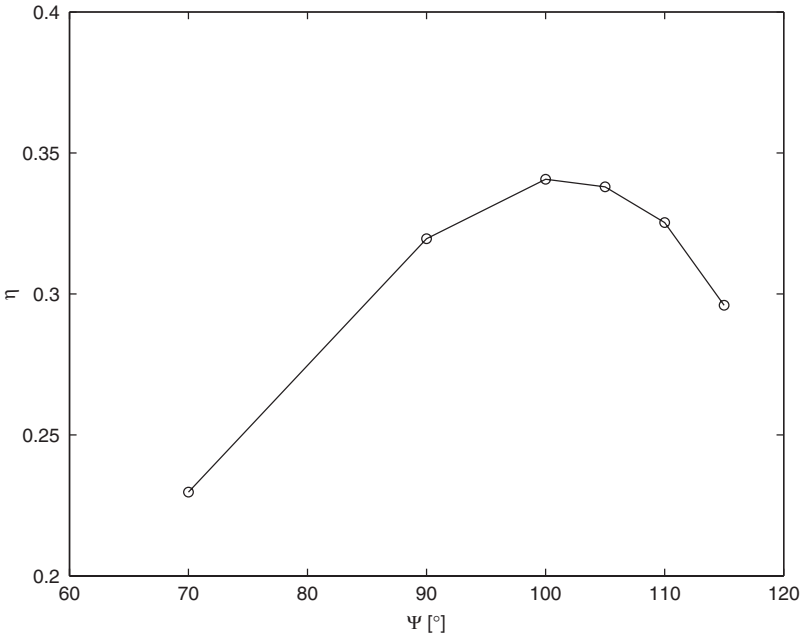

Figure 23. Average thrust coefficient versus phase angle; $h_0/c = 0.5$, $\theta_0 = 30^\circ$, $St_h = 0.25$.

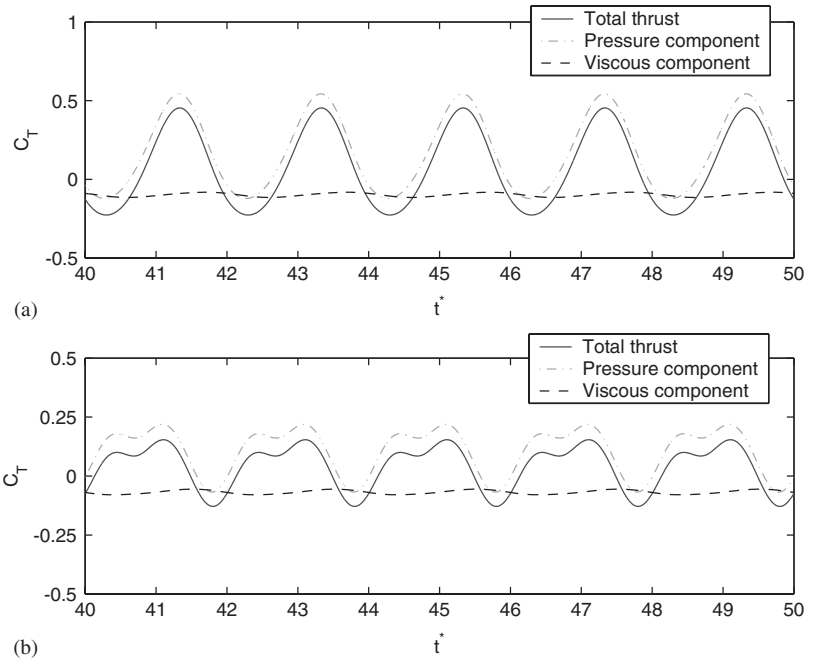

Figure 24. Thrust coefficient versus time for $\Psi = 90^\circ$ (a) and $\Psi = 70^\circ$ (b); $h_0/c = 0.5$, $\theta_0 = 30^\circ$, $St_h = 0.25$.

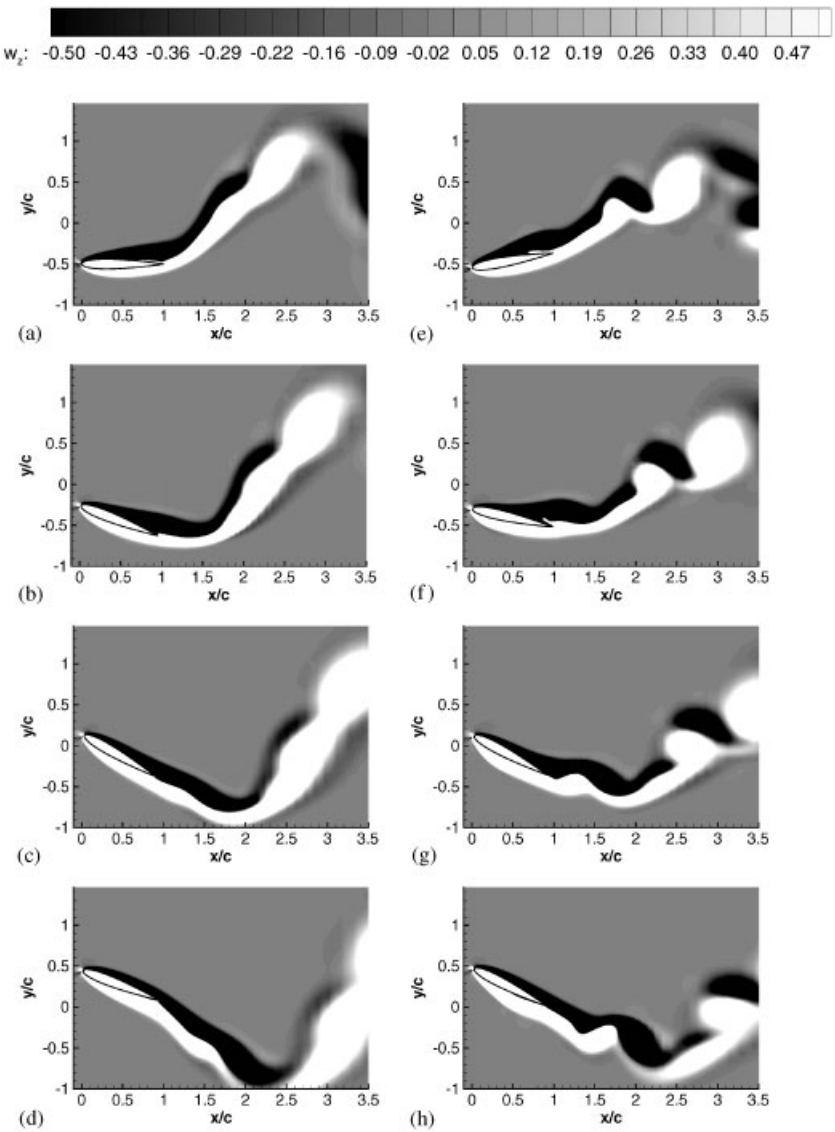

Figure 25. Vorticity plot over half a cycle (snapshots at $t = 0$, $0.125T$, $0.25T$ and $0.375T$) for cases PSI4 (a)–(d) and PSI3 (e)–(h). In PSI4, the phase angle is set to 90°, while in PSI3 the phase angle is 70°.

When the reverse Kármán vortex street is orderly, it increases not only the efficiency but also thrust. The more compact and coherent the vortices are when they are created, the less energy is wasted in creating them. As was shown in this section, the creation of secondary vortices as well as a break up of the main shed vortex by its twin increases energy loss.

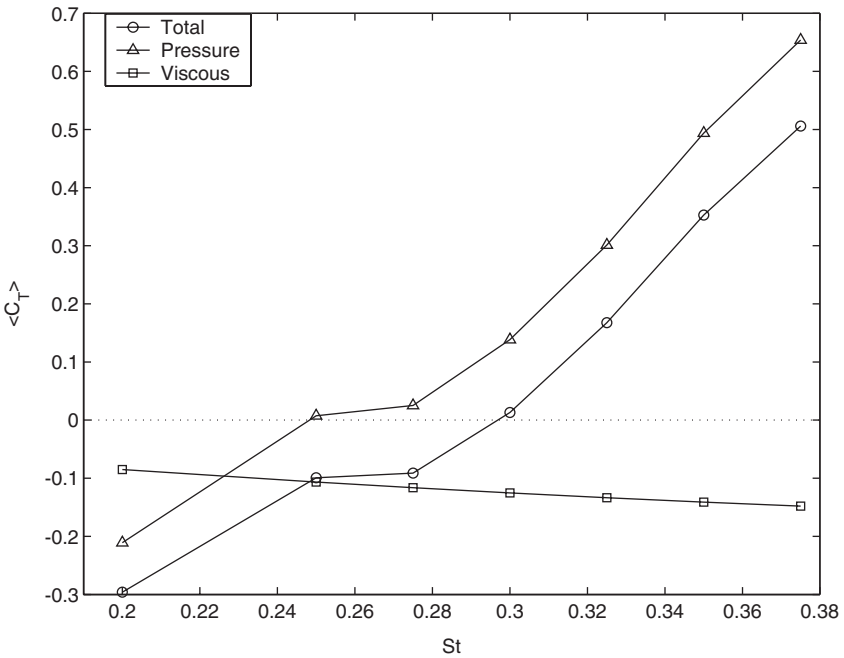

Figure 26. Average thrust coefficient versus Strouhal number; $\Psi = 100^\circ$, $\theta_0 = 40^\circ$, $h_0/c = 0.5$.

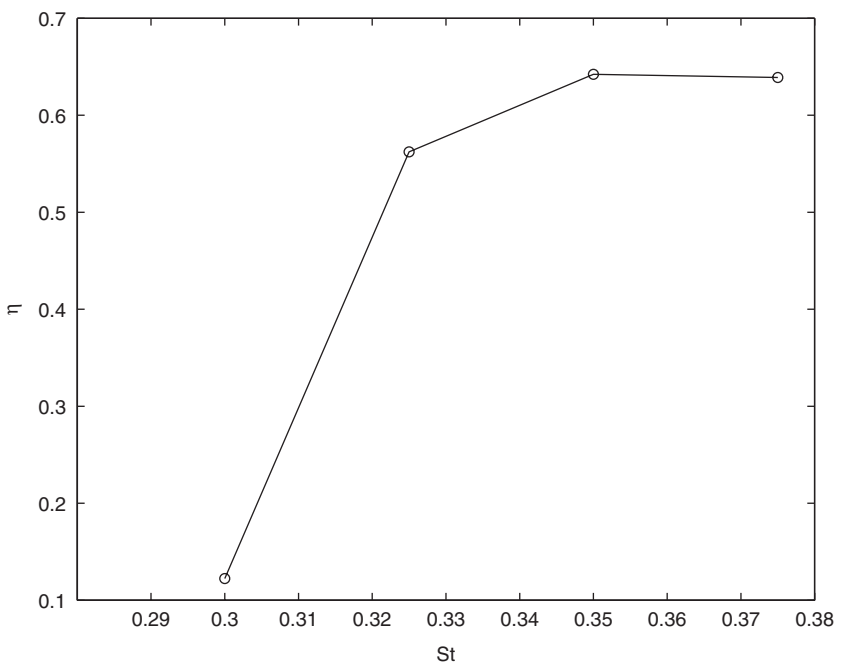

Figure 27. Efficiency versus Strouhal number; $\Psi = 100^\circ$, $\theta_0 = 40^\circ$, $h_0/c = 0.5$.

Some of the simulations performed in this chapter can be directly compared with results obtained in Anderson's study of flapping hydrofoils [17, 28]. Her study consisted of towing a hydrofoil undergoing a pitching and heaving motion. Two Reynolds number were considered: 40 000 and 1100. In the former, it was possible to measure the moment on the hydrofoil and the associated power and efficiency. In the lower Reynolds number case, this was not done and comparison to our simulations is only possible for thrust. In all cases, the present study underpredicted the thrust from about 15–40% in the worst case. The discrepancies are attributed to some extent to insufficient grid refinement, but primarily to three-dimensional effects that are not accounted for in the present simulations.

6. CONCLUSIONS

The CFD-based method is an excellent numerical tool to solve the flow field using the full Navier–Stokes equations and complex geometries can be easily incorporated. With these advantages comes greater computational effort and the need for a more judicious choice of simulation parameters. The mechanism of thrust generated by a flapping hydrofoil was represented by a two-dimensional flow at low Reynolds numbers. In this range, smaller grids can be used to reduce the computational time needed to solve the flow field. A drawback in simulating flows at low Reynolds numbers is that the viscous forces are overestimated in relation to the high Reynolds number flows calculations. At a Reynolds number in which the craft will operate thrust and lift forces due to viscosity are very small compared to the inertial forces. This means that the maximum efficiency calculated can be improved upon by simply increasing the Reynolds number. Experimental tests by Anderson *et al.* [17] at a Reynolds number of 40 000 shows runs with 90% efficiency, thus validating this observation.

The code validation was performed using an oscillating cylinder in a cross-flow. This type of flow is similar to the one generated by the oscillating hydrofoil, as shown in the flow visualization results. Also, this benchmark case helped validate the ALE algorithm close to solid boundaries. The results reported in the literature for this case vary considerably however CFDLIB produced results which fitted into the solution set.

The results obtained show the sensitivity of thrust and efficiency to the Strouhal number, maximum pitch angle and phase angle. This is an important result that has to be taken into account when designing the prototype. A design trade-off was found between the efficiency and generated thrust. Although efficiency is an obvious parameter to maximize, one might not want to do it at a cost of reducing thrust, as acceleration is often an important design consideration in the operational envelope of the undersea vehicle.

The simulations revealed that the maximum lift coefficient decreases with increasing pitch angle. The operation point was selected based on the need for greater thrust without sacrificing efficiency. A maximum pitching angle of 30° was found to be optimal. It was found that a small variation in oscillation frequency considerably affected thrust and efficiency. An increase in oscillation frequency resulted in an increase in average thrust, maximum lift and average power. The effect of phase angle between the heaving and pitching motions was studied as well. It was found that the average thrust coefficient increases with the phase angle. Below 60° the average thrust is negative, resulting in drag. The maximum lift coefficient has a minimum at 70° and then it increases rapidly while the thrust is positive. The hydrofoil was found to generate positive thrust between these two operating values. The performance

of the hydrofoil does not depend on the heaving frequency and amplitude, however it was found to depend on the Strouhal number. A small variation in the Strouhal number can have an extremely large effect on the thrust and efficiency.

Finally, the efficiency was maximized based on the simulations results from the parametric analysis. In order to maximize efficiency, the design variables were set at the optimum values, i.e. maximum pitching angle at 40°, phase angle at 100° and non-dimensional heaving amplitude at 0.5. The Strouhal number was varied by changing the oscillation frequency. It was found that efficiency was a maximum at a Strouhal number of 0.35, with a value of 64% .

ACKNOWLEDGEMENTS

We like to acknowledge the Fluid Dynamics group at Los Alamos for allowing the use of CFDLib and the super computing facility, Minerva, at the University of Victoria.

REFERENCES

1. Triantafyllou GS, Triantafyllou MS, Grosenbaugh MA. Optimal thrust development in oscillating foils with application to fish propulsion. *Journal of Fluids and Structures* 1993; **7**:205–225.
2. Lighthill MJ. Note on the swimming of slender fish. *Journal of Fluid Mechanics* 1960; **9**:305–317.
3. Katz J, Weihs D. Hydrodynamic propulsion by large amplitude oscillation of an airfoil with chordwise flexibility. *Journal of Fluid Mechanics* 1978; **88**:485–497.
4. Wu TY. Swimming of a waving plate. *Journal of Fluid Mechanics* 1961; **10**:321–344.
5. Siekmann J. Theoretical studies of sea animal locomotion, Part I. *Ingenieur-Archiv* 1962; **31**:214–228.
6. Uldrick JP, Siekmann J. On the swimming of a flexible plate of arbitrary finite thickness. *Journal of Fluid Mechanics* 1964; **20**:1–33.
7. Wu TY. Hydromechanics of swimming propulsion. Part 1. Swimming of a two-dimensional flexible plate at variable speeds in an inviscid fluid. *Journal of Fluid Mechanics* 1971; **46**:337–355.
8. Wu TY. Hydromechanics of swimming propulsion. Part 2. Some optimum shape problems. *Journal of Fluid Mechanics* 1971; **46**:521–544.
9. Cheng JY, Zhuang LX, Tong BG. Analysis of swimming three-dimensional plates. *Journal of Fluid Mechanics* 1991; **232**:341–355.
10. Bandyopadhyay PR, Castano JM, Rice JQ, Philips RB, Nedderman WH, Macy WK. Low-speed maneuvering hydrodynamics of fish and small underwater vehicles. *Journal of Fluids Engineering—Transactions of the American Society of Mechanical Engineers* 1997; **119**:136–144.
11. Isshiki H, Murakami M. A theory of wave devouring propulsion. *Society of Naval Architects of Japan* 1984; **156**:102–114.
12. Koochesfahani M. Vortical patterns in the wake of an oscillating airfoil. *AIAA Journal* 1989; **27**:1200–1205.
13. Triantafyllou MS, Triantafyllou GS, Gopalkrishnan R. Wake mechanics for thrust generation in oscillating foils. *Physics of Fluids A* 1991; **3**(12):2835–2837.
14. Gopalkrishnan R, Triantafyllou MS, Triantafyllou GS, Barrett D. Active vorticity control in a shear flow using a flapping foil. *Journal of Fluid Mechanics* 1994; **274**:1–21.
15. Ramamurti R, Sandberg W, Löhner R. Simulation of flow about flapping airfoils using a finite element incompressible flow solver. In *37th AIAA Aerospace Sciences Meeting and Exhibit*, American Institute of Aeronautics and Astronautics, Reno, NV, 1999.
16. Tuncer IH, Platzer MF. Computational study of flapping airfoil aerodynamics. *Journal of Aircraft* 2000; **37**(3):514–520.
17. Anderson JM. Vorticity control for efficient propulsion. *PhD thesis*, Massachusetts Institute of Technology/Woods Hole Oceanographic Institution, 1996, pp. 83–145.
18. Stix G. RoboT. *Scientific American* 1994; **270**.
19. Brackbill JU, Johnson NL, Kashiwa BA, Vanderheyden WB (eds). *Workshop*: *Multi-Phase Flows and Particle Methods*. CFD Society of Canada: Victoria, BC, 1997.
20. Blackburn HM, Henderson RD. A study of two-dimensional flow past an oscillating cylinder. *Journal of Fluid Mechanics* 1999; **385**:255–286.
21. Mendes PA, Branco FA. Analysis of fluid–structure interaction by an arbitrary Lagrangian–Eulerian finite element formulation. *International Journal for Numerical Methods in Fluids* 1999; **30**:897–919.

22. Koopman GH. The vortex wakes of vibrating cylinders at low Reynolds numbers. *Journal of Fluid Mechanics* 1967; **28**:501–512.
23. Tanida Y, Okajima A, Watanabe Y. Stability of a circular cylinder oscillating in uniform flow or in a wake. *Journal of Fluid Mechanics* 1973; **61**(4):769–784.
24. Mittal S, Tezduyar TE. A finite element study of incompressible flows past oscillating cylinders and aerofoils. *International Journal for Numerical Methods in Fluids* 1992; **15**(9):1073–1118.
25. Mittal S, Tezduyar TE. Massively parallel finite element computation of incompressible flows involving fluid-body interactions. *Computer Methods in Applied Mechanics and Engineering* 1994; **21**(3–4):253–282.
26. Tezduyar TE. Parallel finite element simulation of 3D incompressible flows: fluid–structure interactions. *International Journal for Numerical Methods in Fluids* 1995; **21**(10):933–953.
27. Hirt CW, Amsden AA, Cook JL. An arbitrary Lagrangian–Eulerian computing method for all flow speeds. *Journal of Computational Physics* 1974; **14**.
28. Anderson JM, Streitlien K, Barrett DS, Triantafyllou MS. Oscillating foils of high propulsive efficiency. *Journal of Fluid Mechanics* 1998; **360**:41–72.

